

Earth-based observations of impact phenomena

By PHILIP D. NICHOLSON

Department of Astronomy, Cornell University, Ithaca, NY, 14853, USA

Earth-based observations at near- and mid-infrared wavelengths were obtained for at least 15 of the SL9 impacts, ranging from the spectacular G, K and L events to the barely-detected N and V impacts. Although there were a few exceptions, most of the IR lightcurves fit a common pattern of one or two relatively faint precursor flashes, followed several minutes later by the main infrared event as the explosively-ejected plume crashed down onto the jovian atmosphere. Correlations with the impact times recorded by the Galileo spacecraft and plumes imaged by the Hubble Space Telescope lead to an interpretation of the twin precursors in terms of (i) the entry of the bolide into the upper atmosphere, and (ii) the re-appearance of the rising fireball above Jupiter's limb. Positive correlations are observed between the peak IR flux observed during the splashback phase and both pre-impact size estimates for the individual SL9 fragments and the scale of the resulting ejecta deposits. None of the fragments observed to have moved off the main train of the comet by May 1994 produced a significant impact signature. Earth-based fireball temperature estimates are on the order of 750 K, 30–60 sec after impact. For the larger impacts, the unexpectedly protracted fireball emission at 2.3 μm remains unexplained. A wide range of temperatures has been inferred for the splashback phase, where shocks are expected to have heated the re-entering plume material at least briefly to several thousand K, and further modelling is required to reconcile these data.

1. Introduction

The impacts of the 20 or so fragments of comet Shoemaker-Levy 9 (henceforth SL9 for simplicity) with Jupiter in July 1994 were observed from a wide range of Earth-based telescopes, including instruments in Europe, South and North America, Hawaii, Australia, Japan, South Africa and even Antarctica. In this review we will concentrate on Earth-based near-infrared and mid-infrared observations of prompt phenomena, defined as those occurring within approximately one hour after the impacts. The extensive sets of post-impact imaging and spectroscopic studies of the impact sites, including compositional analyses of the impact debris, are reviewed in the chapters by West, Lellouch, Moses, and Conrath. Magnetospheric effects are reviewed in the chapter by Ip.

The most extensive sets of ground-based data were obtained in the near-infrared, especially at wavelengths of 2.3 and 3.5 μm where methane absorption bands in the jovian spectrum greatly reduce the planetary background and enhance the contrast of the impact features. By a fortunate coincidence, this spectral region was also near the peak of thermal emission from the impact plumes and their remnants. A new generation of infrared cameras and spectrometers provided the bulk of the data, and we may reflect upon our good fortune that the impact of SL9 did not occur a decade earlier.

Although Jupiter rose in the early afternoon and set before midnight at most sites (the notable exception being the South Pole station where almost continuous monitoring was possible), the wide geographical distribution of observers ensured that attempts were made to observe every predicted impact. Of the 24 predicted impacts (Sekanina *et al.* 1994; Chodas & Yeomans 1994 [email predictions]), convincing detections of 15 have been reported to date, and another three (B, M and U) may have been marginally detected. Six fragments (F, G2, J, P1, P2 and T) appear either to have disintegrated completely

before encountering Jupiter, or to have disappeared into the planet's atmosphere without a trace.

After a discussion of a typical SL9 lightcurve, and what has become the standard interpretation of its main features, we begin in §2 by summarizing the observed phenomena and classifying the impacts into five categories. In §3 we present a detailed description of the successive phases in a generic lightcurve, drawing on individual examples for illustrations. An attempt is made to relate these observations to those made simultaneously by the Galileo spacecraft (see chapter by Chapman in this volume) and by the Hubble Space Telescope (see chapter by Hammel). A simple ballistic model of the impact plumes which is consistent with the ensemble of observed lightcurves is used as common framework for interpretation of the observations. This model is based loosely on the numerical models developed in the chapters by Crawford, Zahnle and MacLow. In §4 we discuss the relatively small number of spectroscopic observations made during the actual impact events, and their interpretation in terms of plume and fallback temperatures. Sections 5 and 6 cover other prompt phenomena associated with the impacts, while in §7 we summarize our conclusions.

1.1. *A typical example: the R impact*

Most, if not all, of the features seen in the near-infrared SL9 impact lightcurves are illustrated in the data obtained for the medium-sized R impact and shown in Figure 1. The 2.3 μm observations were made at Mauna Kea with the Keck 10m telescope and the near-IR camera (Graham *et al.* 1995), while the 3.2 and 4.5 μm observations were made at the 5m Hale telescope at Palomar, using simultaneously-mounted near-IR and mid-IR cameras (Nicholson *et al.* 1995a). Sampling times were 8–10 sec at 2.3 and 4.5 μm and 30 sec at 3.2 μm . The 4.5 μm fluxes have been corrected for background light from Jupiter, but the steady pre-impact slope in the 2.3 μm data is due to the rotation of the older G impact site onto the jovian limb. Black bars under the lightcurves indicate the times (corrected for light travel time) during which the Galileo NIMS instrument observed detectable flux from the impact (Carlson *et al.* 1995b).

Shortly before the initial Galileo flash, a brief flash was observed at all three wavelengths with a duration of ~ 30 sec. About 60 sec after the first signal, a second, brighter flash began abruptly, only to decay over the next minute or so (within 30 sec at 4.5 μm , but extending over 3 min at 2.3 μm). These two events have come to be known as the *first* and *second precursors*, respectively. The precursor events are shown at an expanded scale in Fig. 1(b). Approximately 6 min after the initial flash a dramatic brightening commenced, eventually reaching a peak flux about one hundred times greater than that of the second precursor, 10 min after the impact. This *main event* was observed simultaneously by earth-based telescopes and by Galileo NIMS. Following the peak of the main event the infrared flux decayed with a time constant of ~ 3 min. This fading was interrupted by a *shoulder*, or secondary maximum, occurring ~ 9 min after the peak. At 3.2 μm there is an indication of a second, weaker shoulder ~ 18 min after the main peak.

The generic sequence of events represented by this lightcurve is illustrated schematically in Fig. 1 in the chapter by Zahnle, and in Fig. 2 of Boslough *et al.* (1995). Figure 2 shows the particular geometry for earth-based observations of the R impact. As seen from Earth, the impact itself occurred $\sim 5.7^\circ$ in longitude behind the planet's dawn limb; the events were observed directly only by Galileo. The first precursor apparently corresponded to thermal emission from the trail left by the passage of the fragment through Jupiter's upper atmosphere, and was too faint to be detected by the less-sensitive Galileo instruments. About 30 sec after Galileo observed the intensely bright terminal phase of the impact, the expanding, incandescent fireball rose above the limb into our

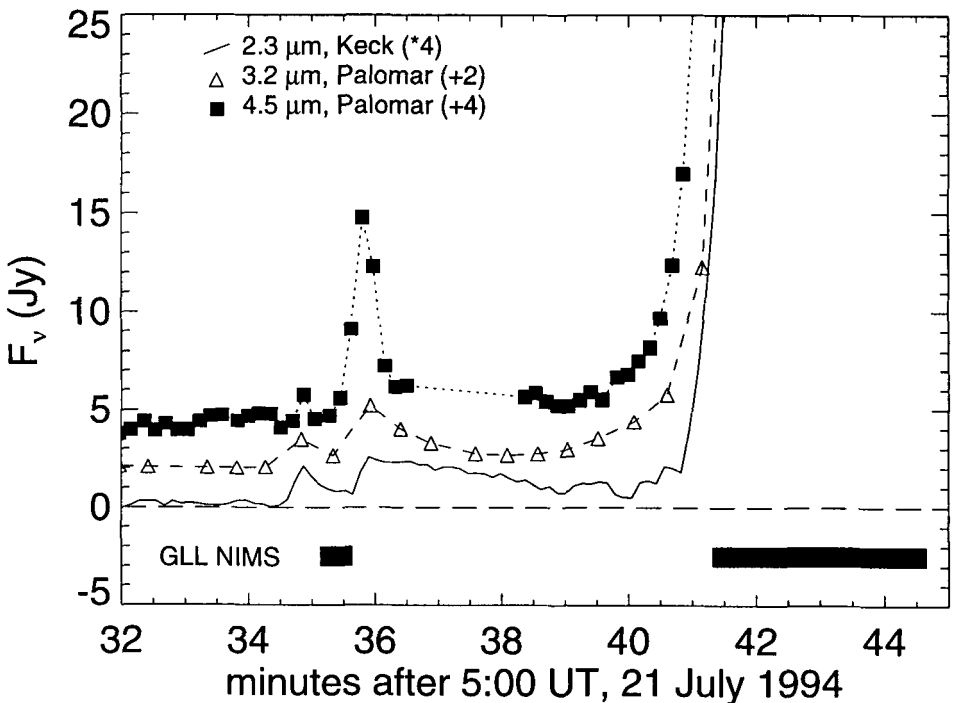
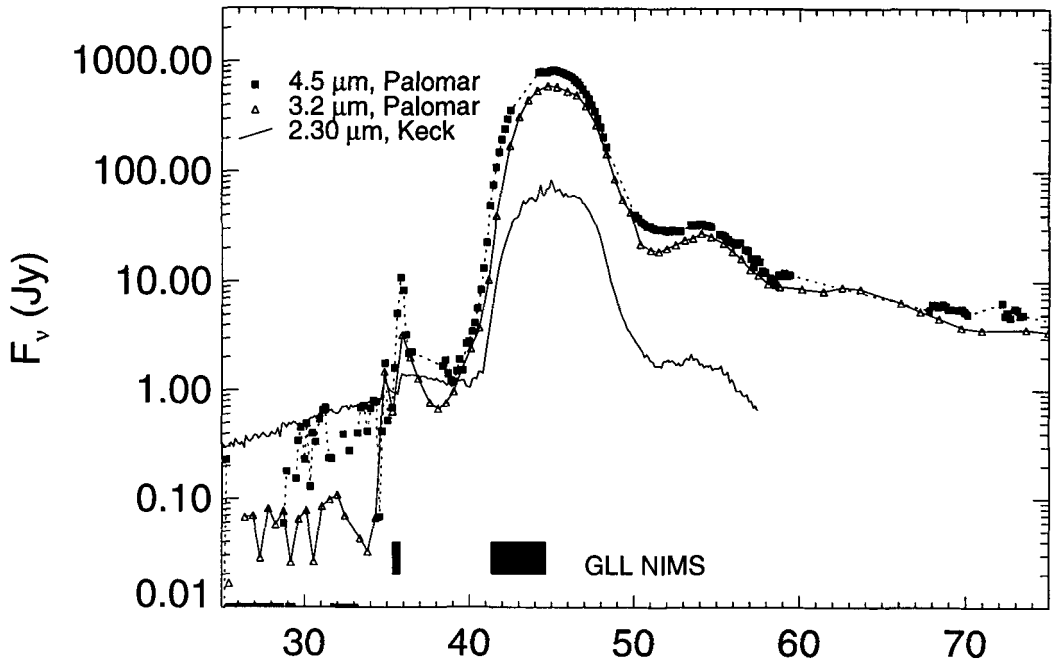


FIGURE 1. (a) Lightcurves for the R impact, as observed at the Keck 10m and Palomar 5m telescopes, on a logarithmic scale. Gaps in the 4.5 μm data correspond to periods during which spectroscopic measurements were obtained. Solid black bars indicate the periods of emission observed by the Galileo NIMS instrument. (b) Expanded plot of the R precursor events on a linear scale. Note the scale factor applied to the 2.3 μm data.

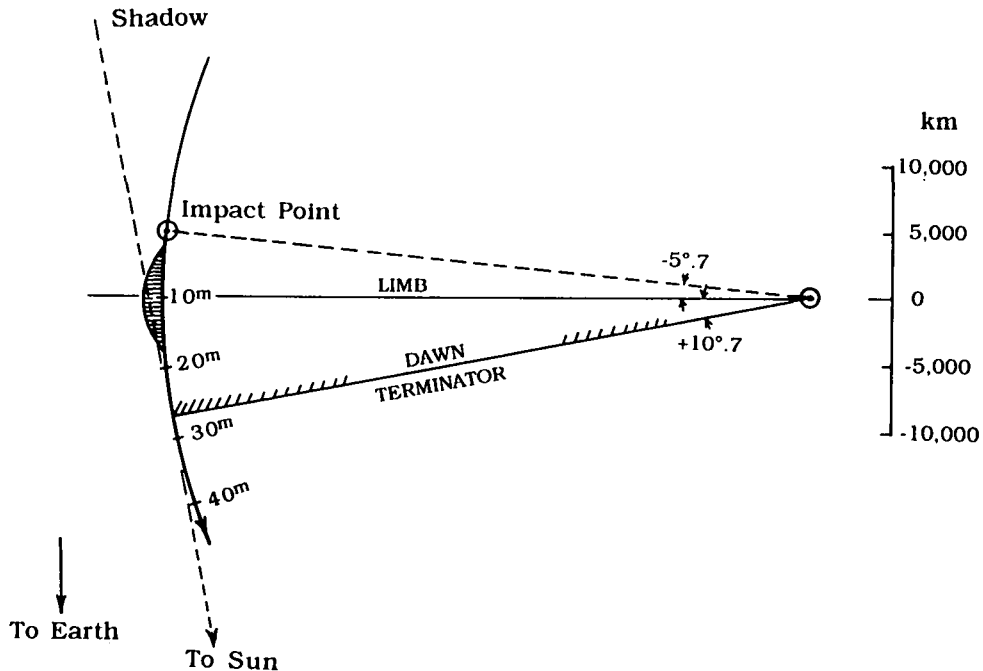


FIGURE 2. Geometry for earth-based observations of the R impact. The diagram shows the view from above Jupiter's north pole, with the Earth towards the bottom of the page and the planet's center towards the right edge. The R impact site, indicated by the \odot symbol, was behind the limb and out of direct sight. Ten min after the impact, and near the time of peak IR flux, the site reached the limb. The plume was also near its maximum height, as indicated schematically by the hatched region. Another 17 min elapsed before the impact site reached the dawn terminator and direct sunlight. The geometry for the other impacts was similar, with earlier impacts generally occurring further behind the limb and later impacts even closer (Sekanina *et al.* 1994).

line of sight, although still in the pre-dawn shadow. This is the second precursor, whose decay represents the rapidly cooling fireball. Now quite cold, but emerging after 1–2 min into sunlight and visibility by the Hubble Space Telescope (henceforth HST), the debris plume reached a maximum altitude of ~ 3200 km above Jupiter's cloud tops (Hammel *et al.* 1995), before falling back into the planet's atmosphere. (This is based on observations of other impacts; HST did not observe the R impact.) For R, the maximum height was reached just as the impact site itself rotated into view, but this was not the case for earlier impacts, which occurred further behind the limb. The infrared main event corresponds to this extended period of fallback, which lasted from 6 to ~ 15 min after the impact, and during which the descending debris was shock-heated again to temperatures of at least 500–1000 K, and perhaps much higher.

The origin of the secondary shoulders is less certain, but they may be due to re-entering material 'bouncing' off the top of the atmosphere and re-entering a second (or even a third) time (Deming *et al.* 1995). Not until ~ 27 min after the impact did the R impact site cross the dawn terminator and emerge into direct sunlight. In practice, it is impossible to distinguish in near-IR images of the impacts between the dying thermal stages of the main event and the appearance of the fresh impact site in reflected sunlight on the terminator.

With minor modifications, this scenario seems to fit the observations of almost all of the impacts, while also being consistent with numerical models of the process of fireball formation and evolution (Boslough *et al.* 1994; Crawford *et al.* 1994; Zahnle & MacLow 1994; Takata *et al.* 1994). We will use it as a working model in describing some of the detailed features exhibited by other lightcurves in § 3 below.

2. Lightcurve classification

2.1. Lightcurve comparisons

Comparison of lightcurves for different events is often complicated by differences in telescope aperture, wavelength of observation, sampling time and weather conditions. Two extensive series of homogeneous observations which avoid these pitfalls are shown in Figs. 3 and 4. Figure 3, from McGregor *et al.* (1995), presents near-IR lightcurves obtained at the 2.3 m telescope at Siding Spring Observatory, Australia for events C, D, G, K, R and W. Impact N was detected only weakly in 3 frames, while V was not detected at all. The data were obtained with the CASPIR near-IR camera, at exposure intervals of ~ 50 sec, using a narrow-band $2.34 \mu\text{m}$ filter. These data include examples of large, medium-size and small impacts, and in addition to precursors for events C, D, G, K and W, the lightcurves show prominent shoulders for C, D and G. (The lightcurves for the later impacts were followed only through the main peak.)

Figure 4, from Lagage *et al.* (1995), presents a series of mid-IR lightcurves for the A, E, H, L and Q1 impacts obtained with the $10 \mu\text{m}$ CAMIRAS camera at the 2.6 m Nordic Optical Telescope at La Palma, in the Canary Islands. Impacts F, P2, Q2, T and U were not detected. The filter passband was $10.5\text{--}13 \mu\text{m}$, and the original 1.1 sec samples have been binned at intervals of ~ 60 sec. The background thermal emission from Jupiter has been subtracted from the images. The lightcurve for the extremely bright L impact also shows a brief precursor ~ 60 sec after the Galileo flash, with a peak flux of 300 Jy. A similar precursor was seen at $10 \mu\text{m}$ for the H impact by Livengood *et al.* (1995), using the TIMMI camera at the ESO 3.6 m telescope at La Silla, Chile. Although not prominent in this presentation, each of the lightcurves shows a definite shoulder ~ 20 min after the impact. The shoulders are most prominent for H and L.

2.2. Summary of observations

Table 1, compiled by P. Chodas from published reports and a survey of participants at IAU Colloquium 156, and with some additions by the author, summarizes the observed phenomena associated with each impact. The adopted impact times are based on Galileo observations of the initial flash where available, on Earth-based precursor times, or—where necessary—on predictions or extrapolation from the onset of the of the main event. For further details the chapter by Chodas & Yeomans should be consulted. PC1 and PC2 refer to detections of the first and second precursors, respectively, and ME to observations of the infrared main event. The columns labelled ‘spot’ and ‘ejecta’ refer to the presence of these features in HST images (Hammel *et al.* 1995). The last two columns give the morphological class assigned by Hammel *et al.*, which reflects a combination of characteristics such as central spot size, scale of ejecta blanket, and prominence of waves (if any), and the Galileo instruments which observed the event, where applicable.

In Fig. 5 we plot the main event peak flux at $2.3 \mu\text{m}$, a quantity which is available for most of the observed impacts from published lightcurves, vs. the HST class. On the basis of this diagram, and on the observability of the post-impact features in ground-based images of Jupiter, the impacts can be fairly cleanly (if somewhat arbitrarily) divided into five categories.

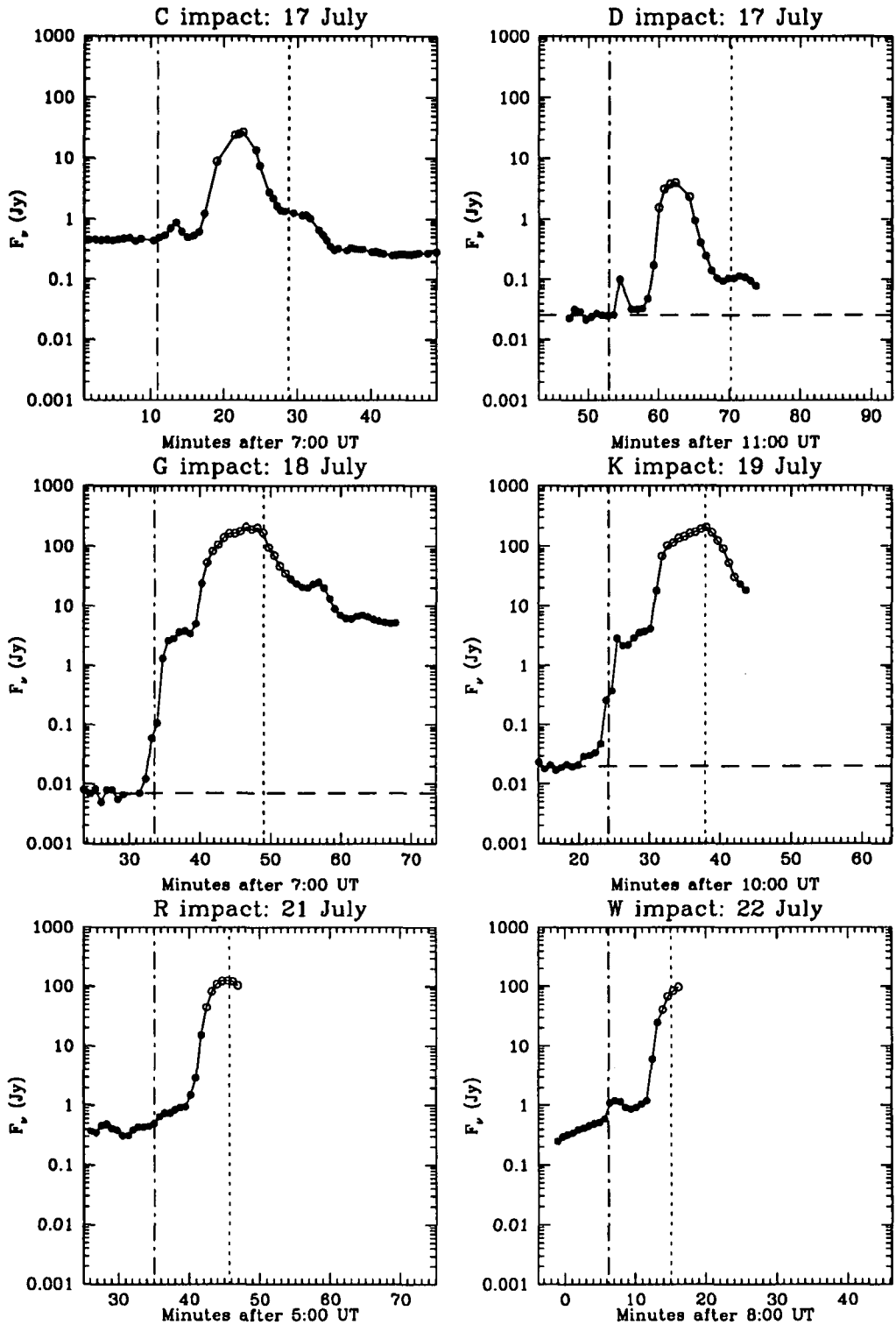


FIGURE 3. Lightcurves at $2.34 \mu\text{m}$ obtained at Siding Spring Observatory, Australia. Open symbols indicate frames in which the brightest part of the image exceeded the linear range of the detector, and the total flux is likely to be underestimated. Vertical dot-dashed lines indicate the adopted impact times from Table 1, while vertical dashed lines indicate the time at which the impact site reached the planet's limb (see Fig. 2). From McGregor *et al.* (1995).

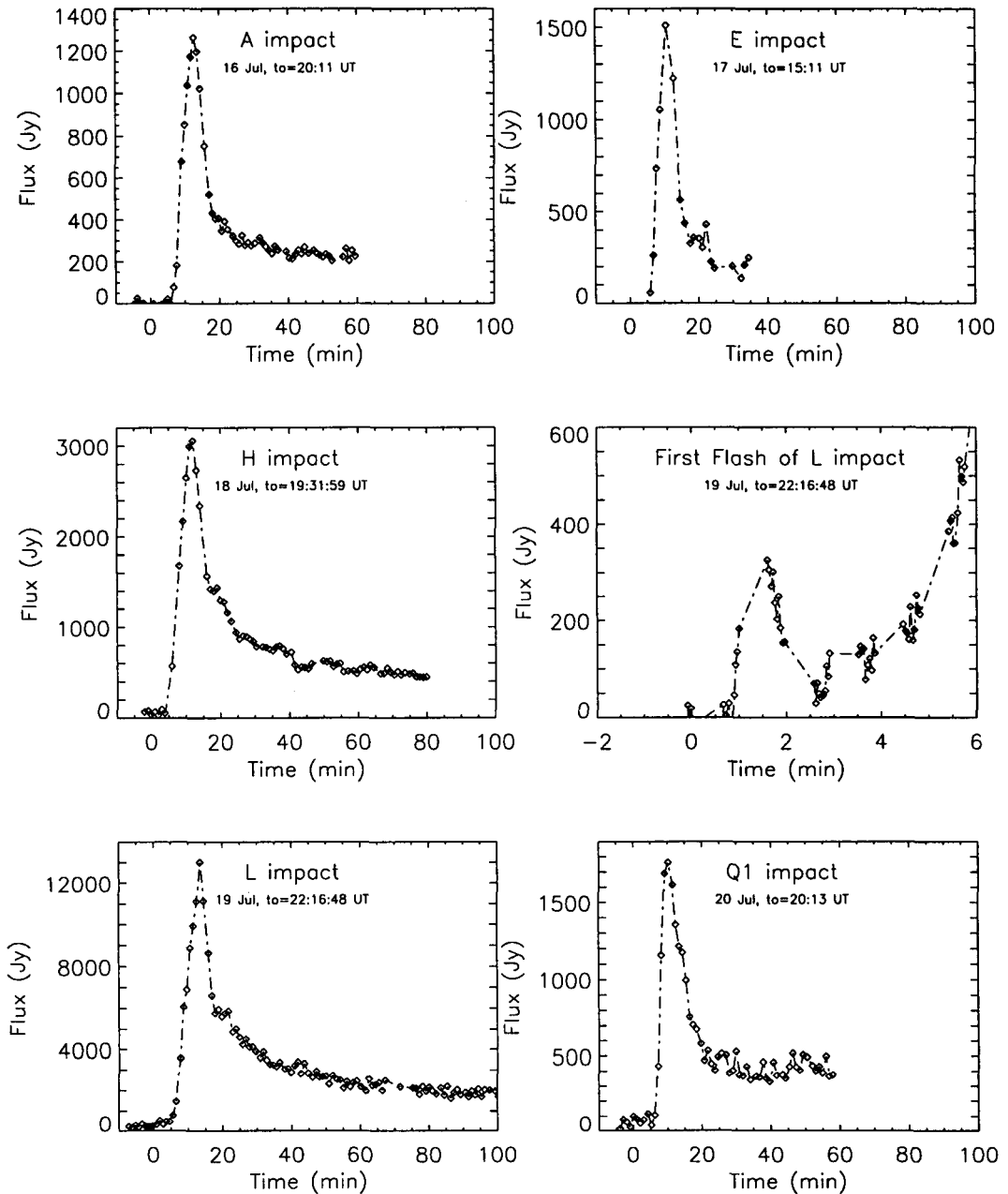


FIGURE 4. Lightcurves at $12\ \mu\text{m}$ obtained at La Palma in the Canary Islands. The abscissa is time from the nominal impact time, as indicated in each panel. From Lagae *et al.* (1995).

(i) Large impacts G, K and L produced peak IR fluxes of 200 Jy or greater, and were associated with prominent post-impact sites visible in both the HST images and in Earth-based near-IR images.

(ii) Medium-sized impacts (peak fluxes in the range 50–200 Jy) include E, H, Q1, R, S and W. All except S and W (which landed very close to the already complex G and K sites and were difficult to distinguish as a result) produced post-impact features of class 2 in the HST images, which were also readily detectable in Earth-based images.

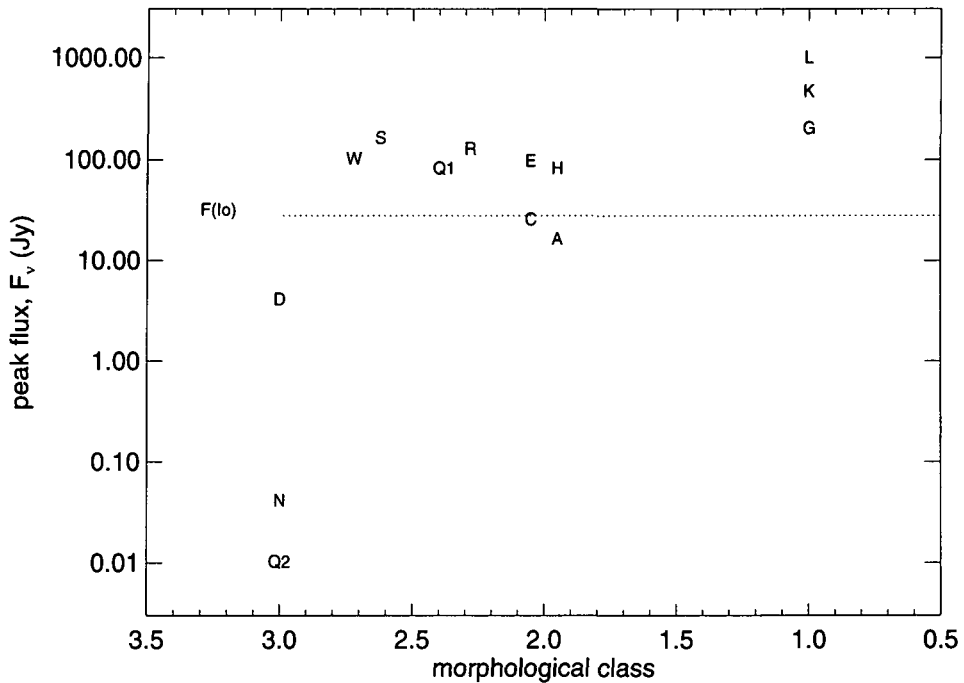


FIGURE 5. Comparison of main-event peak flux at $2.3 \mu\text{m}$ vs. impact classification based on HST images by Hammel *et al.* (1995). Near-IR data from various sources. In some cases approximate corrections have been made to allow for detector saturation.

(iii) Impacts A, C and D we classify as small, due to their smaller peak near-IR fluxes of 5–20 Jy, and to the comparative faintness of the impact sites in Earth-based near-IR images. The D site was, in fact, indistinguishable from the nearby G site in most ground-based images. However, both A and C were rated as class 2a on the basis of HST images, and the peak $12 \mu\text{m}$ flux from the A impact was comparable to that seen for E and Q1 (cf. Fig. 4).

(iv) Impacts B, M, N, Q2, U and V we classify as ‘wimps’, due to very faint and/or uncertain detections of the impacts themselves. For none of these impacts was a remnant detectable in Earth-based near-IR images of Jupiter, and only sites B, N and Q2 were detectable in the higher-resolution HST images. Impacts B and M were detected only by the Keck telescope. Q2 produced an obvious precursor, but a very weak main event. V appears to have been unique in that a precursor event was observed at two stations, but with no subsequent main event. Impact U is questionable, given at least two negative reports from larger telescopes. See §5 for further details on these events.

(v) No credible reports of impact signatures exist for fragments F, G2, J, P1, P2 and T, and there are no identifiable impact sites corresponding to the predicted impact locations in the HST images. Fragments J and M had in fact disappeared at least six months prior to July 1994, while fragments P1 and P2 had been observed to be further disintegrating (Weaver *et al.* 1995).

It is also of interest to compare the luminosities of the impact events with the relative sizes of the fragments inferred from their brightness in pre-impact HST images (Weaver *et al.* 1995). In Fig. 6 we make such a comparison, again using the peak $2.3 \mu\text{m}$ flux as a yardstick. (A’Hearn *et al.* (1995) present a similar plot using peak and integrated Galileo fluxes at $0.945 \mu\text{m}$.) On average, the peak luminosity is roughly proportional to the cube of the estimated pre-impact diameter, *i.e.*, to the putative mass and ki-

Fragment	Date/time (UT)	PC1	PC2	ME	Spot	Ejecta	HST	Galileo
A	July 16, 20:12	–	Y	Y	Y	Y	2a	–
B	July 17, 02:50	–	–	?	Y	–	3	–
C	July 17, 07:11	–	Y	Y	Y	Y	2a	–
D	July 17, 11:53	–	Y	Y	Y	–	3	–
E	July 17, 15:12	–	–	Y	Y	Y	2a	–
F	July 18, 00:37	–	–	–	–	–	–	–
G	July 18, 07:33:32	Y	Y	Y	Y	Y	1	UVS/PPR/NIMS
H	July 18, 19:31:59	Y	Y	Y	Y	Y	2a	PPR
J	July 19, 01:35	–	–	–	–	–	–	–
K	July 19, 10:24:13	Y	Y	Y	Y	Y	1	SSI
L	July 19, 22:16:48	Y	Y	Y	Y	Y	1	PPR
M	July 20, 06:02	–	–	?	–	–	–	–
N	July 20, 10:29:17	–	–	Y	Y	–	3	SSI
P2	July 20, 15:23	–	–	–	–	–	–	–
P1	July 20, 16:37	–	–	–	–	–	–	–
Q2	July 20, 19:44	–	Y	Y	Y	–	3	–
Q1	July 20, 20:13:52	–	Y	Y	Y	Y	2b	PPR
R	July 21, 05:35:03	Y	Y	Y	Y	Y	2b	NIMS
S	July 21, 15:16	–	Y	Y	Y	?	2c	–
T	July 21, 18:11	–	–	–	–	–	–	–
U	July 21, 21:56	–	–	?	–	–	–	–
V	July 22, 04:23:10	Y?	–	–	–	–	–	–
W	July 22, 08:06:14	–	Y	Y	Y	?	2c	SSI

TABLE 1. Summary of impact times, observed phenomena, HST impact site classifications and availability of Galileo data for the individual SL9 fragments. PC1 and PC2 refer to Earth-based detections of the first and second precursors, ME to observations of the infrared main event, and ‘spot’ and ‘ejecta’ to the visibility of central spots and crescent-shaped ejecta blankets in the Hubble Space Telescope (HST) images. Question marks refer to uncertain observations, or to the uncertain interpretation of the V event. Galileo instruments are indicated by their standard abbreviations.

netic energy of the fragment, as might be expected. The correlation between fragment size (inferred from their relative brightnesses) and impact flux is, however, by no means a one-to-one relationship. Although the brightest IR signals were associated with the large G, K and L fragments, the impact of the equally-bright Q1 produced an unexpectedly faint infrared signature—and a correspondingly average-sized impact scar on the planet—while the slightly fainter Q2 fragment yielded one of the weakest main events detected. Fragments F, P2, and B might have been expected to produce signatures at least comparable to those readily detected from the smaller A and D fragments.

More significant perhaps is the observation by Weaver *et al.* (1995) that the fragments located off the line of the main SL9 train produced smaller ejecta patterns than their brightnesses would have predicted. These include fragments B, F, G2, N, P2, P1, Q2, T, U and V. If the vanished J and M fragments are included, this list is identical to that of our categories (iv) and (v) above. It seems likely that these fragments were of lower density and much less cohesive than their siblings, perhaps being no more than weakly-bound clumps of debris which entered the jovian atmosphere as meteor showers rather than as coherent bolides.

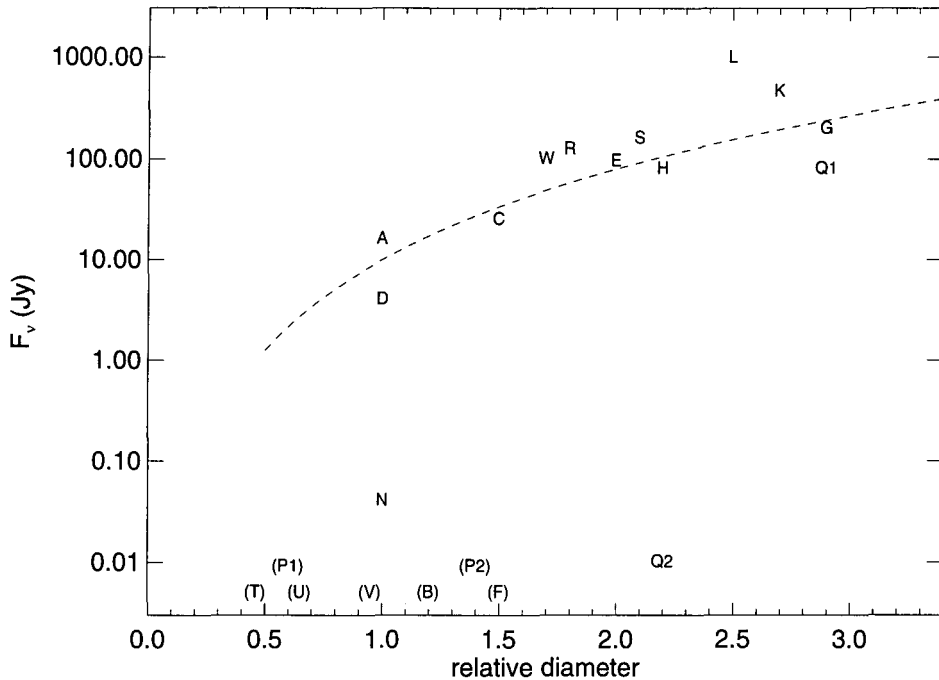


FIGURE 6. Comparison of main-event peak flux at $2.3 \mu\text{m}$ vs. pre-impact relative fragment sizes derived from HST images by Weaver *et al.* (1995). Near-IR data as in Fig. 5. Labels in parentheses indicate either non-detections or very weak detections. The dashed curve is a simple cubic fit.

3. Anatomy of a lightcurve

The various phases in the impact lightcurves are seen most clearly in the R lightcurves in Fig. 1 and in the data from the well-observed G, H, K and L impacts. These lightcurves show very similar characteristics, and we are fortunate in having Galileo observations for all five events, as well as a series of HST images for the G impact. Figures 7 and 8 show the early phases of the G and K impacts, using $2.3 \mu\text{m}$ lightcurves from Siding Spring (McGregor *et al.* 1995) and the Okayama Astrophysical Observatory, Japan (Watanabe *et al.* 1995; Takeuchi *et al.* 1995). In Fig. 7 the periods during which the Galileo PPR, UVS and NIMS instruments observed emission are indicated (Martin *et al.* 1995; Hord *et al.* 1995; Carlson *et al.* 1995a), as are the exposure times of individual HST images (Hammel *et al.* 1995). The period during which the Galileo SSI instrument observed the flash from the K impact (Chapman *et al.* 1995) is shown in Fig. 8.

The early phases of the H and L impacts—the latter being arguably the most energetic of all the SL9 events—are shown in Fig. 9, with lightcurves from the 2.2 and 3.5 m telescopes at Calar Alto, Spain (Hamilton *et al.* 1995) and the 1 m telescope at Pic du Midi, France (Colas *et al.* 1995; Drossart *et al.* 1995). For L, Fig. 9(a) shows a very abrupt first precursor at 22:16:41 UT, followed by a decay over the next 50 sec until the onset of the second precursor at 22:17:30 UT saturated the detector. The Pic du Midi observations in Fig. 9(b) carry the L lightcurve through the second precursor phase, until saturation occurred at the beginning of the main event at about 22:23 UT.

3.1. A simple ballistic model

Although a full understanding of the process whereby the kinetic energy of the incoming fragments of SL9 produced the spectacular events seen by Galileo, HST and Earth-based

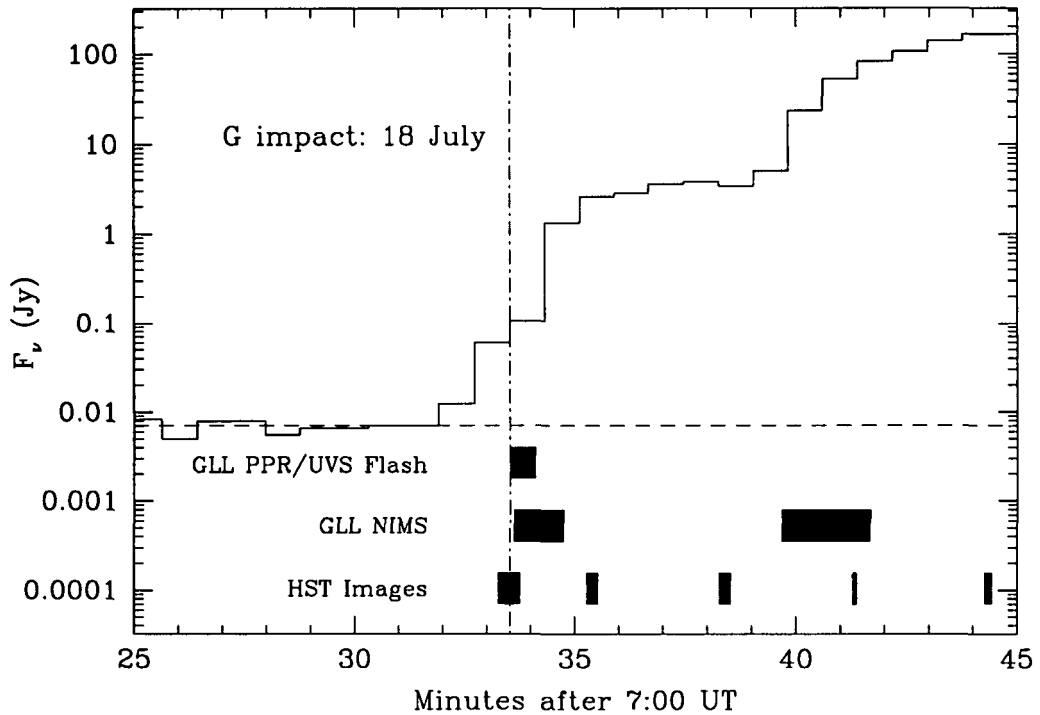


FIGURE 7. Lightcurve for the G impact obtained at Siding Spring Observatory, Australia at $2.34 \mu\text{m}$. Steps indicate individual 30 sec exposures at ~ 50 sec intervals. A vertical dot-dashed line indicates the adopted impact time, as set by the onset of the Galileo PPR/UVS flash. Blocks indicate periods of emission observed by Galileo, and exposure times for HST images. From McGregor *et al.* (1995).

telescopes depends on detailed numerical modelling of the 3-D hydrodynamics of the impact (cf. the chapter by Crawford in this volume), the subsequent evolution of the plumes themselves was largely governed by simple ballistics (see chapters by Zahnle and MacLow). Guided by the observations of maximum plume height and debris distribution by HST (Hammel *et al.* 1995), and the conceptual models of Boslough *et al.* (1995) and Zahnle and MacLow (1995), we can construct a purely ballistic model which accounts for the timing of most of the features seen in the SL9 lightcurves (cf. also Takeuchi *et al.* 1995; Drossart *et al.* 1995).

A maximum vertical ejection velocity for the impact debris cloud of $v_z \simeq 12.5 \text{ km s}^{-1}$ is set by the observed maximum plume height of $v_z^2/2g = 3200 \text{ km}$ (Hammel *et al.* 1995). The 12,500 km outer radius of the 'crescent' of debris seen around the G impact site in HST images (West *et al.* 1995) suggests a maximum ejection velocity of $v_e = \sqrt{gr} \simeq 18 \text{ km s}^{-1}$, although Zahnle has argued that the crescent may have expanded significantly *after* re-entry of the plume material. Both results are consistent with a relatively flat plume trajectory, with a maximum elevation angle $\theta_{\text{max}} \simeq 45^\circ$. An ejection angle of 45° would also match the incoming trajectory of the fragment relative to Jupiter's cloud tops, back along which the bulk of ejecta is predicted to have been ejected (Boslough *et al.* 1995). In reality, of course, the ejecta emerged with a distribution of initial velocities and/or directions, as demonstrated by the broad crescent-shaped ejecta patterns, although the asymmetry of the ejecta blankets seen in the HST images confirms that the plume material was primarily ejected back along the fragments' inbound trajec-

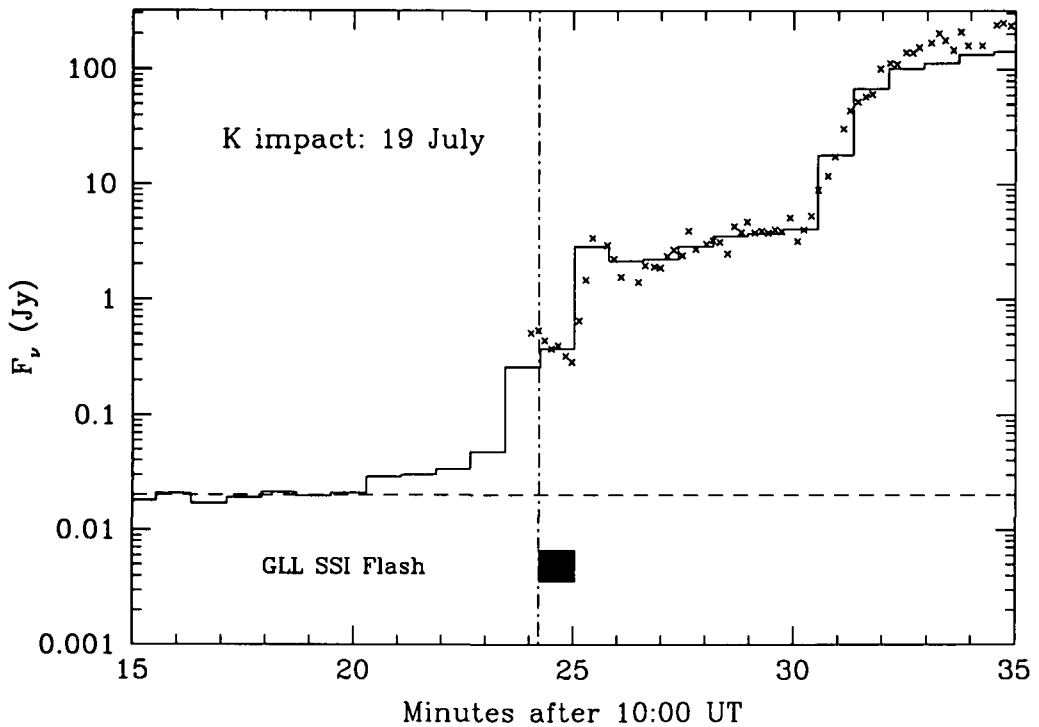


FIGURE 8. Lightcurves for the K impact obtained at Siding Spring Observatory, Australia at $2.34 \mu\text{m}$ (histogram) and the Okayama Astrophysical Observatory, Japan at $2.35 \mu\text{m}$ (crosses). The OAO data are 1 sec exposures taken with an IR camera and narrowband $2.35 \mu\text{m}$ filter, at 10 sec intervals. Neutral density filters were used during the period of peak brightness to avoid detector saturation. A vertical dot-dashed line indicates the adopted impact time, as set by the onset of the Galileo SSI flash. From McGregor *et al.* (1995).

tory, or towards the south-east once allowance is made for Coriolis deflection (Hammel *et al.* 1995).

Figure 10 shows sample trajectories for plume tracers ejected at a common velocity of 18 km s^{-1} and at elevation angles of 15° , 30° and 45° from the horizontal. Superimposed on the particle trajectories are a set of curves indicating the time and altitude at which the ejecta rises above the planet's limb into the view of Earth-based observers, for an ejection azimuth 45° east of south. (These curves also depend weakly on the assumed elevation angle of the ejecta, as they are controlled by both the planet's rotation and the horizontal velocity of the plume: the plotted curves are for $\theta = 30^\circ$.) The different curves for different impacts reflect the varying location of the impact points behind the limb; later impacts generally falling closer to the limb (Chodas & Yeomans, this volume). The G plume, for example, would have become directly visible 32 sec after impact for $\theta = 45^\circ$, whereas the W plume emerged into view after only 12 sec.

The dashed curves in Fig. 10 indicate the time and altitude at which the ejecta rose above the shadow of the jovian limb, and into direct sunlight. Again, the plumes from the later impacts, starting closer to the terminator, rise into sunlight earlier and at a lower altitude. For G, the plume remains in shadow until 130 sec after impact and 1500 km altitude, while for W the interval is only 90 sec and the corresponding altitude $\sim 1000 \text{ km}$, all for $\theta = 45^\circ$. These times are consistent with the sequences of images obtained for these two impacts by HST (Hammel *et al.* 1995): the G plume is seen in

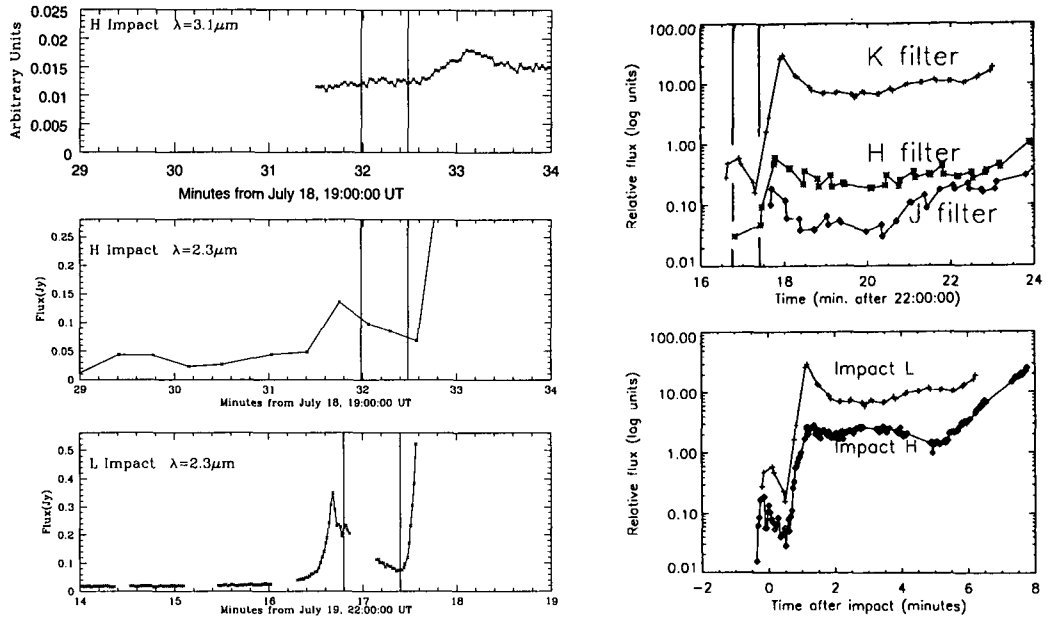


FIGURE 9. (a) Precursor lightcurves for the H and L impacts obtained at the 2.2 and 3.5 m telescopes at Calar Alto Observatory, Spain. The $2.30 \mu\text{m}$ data were obtained with an IR camera and a narrowband methane filter, while the $3.1 \mu\text{m}$ data were obtained with a high-speed photometer. For L the time resolution was 1.2 sec. From Hamilton *et al.* (1995). (b) Lightcurves for the H and L precursors obtained at the 1 m telescope at Pic du Midi Observatory, France. The data were obtained with a multi-channel IR camera and standard *J*, *H* and *K'* (1.25 , 1.65 and $2.12 \mu\text{m}$) filters, at ~ 18 sec intervals. The lower panel compares the $2.12 \mu\text{m}$ data on a common scale. From Colas *et al.* (1995).

thermal emission at $T_i + 2.0$ min and in sunlight at $T_i + 5.0$ min; the W plume is seen emerging into sunlight at $T_i + 3.0$ min.

We now discuss the successive phases in a typical SL9 lightcurve, with this highly simplified but illustrative model as a guide to their interpretation.

3.2. Leader emission

For some minutes prior to the actual impact time, faint emission is seen in the G, K and L lightcurves. This *leader* emission brightens gradually, and then more steeply, until it merges into the first precursor flash. Its duration ranges from ~ 30 sec for L (Fig. 9) to 3.5 min for K (Fig. 8), and is far too long to be accounted for by the passage of the main fragment through Jupiter's atmosphere at the entry velocity of 60 km s^{-1} . More likely, this emission is due to an extended stream of dust preceding the main fragment, which arrived as a 'meteor shower' in Jupiter's atmosphere (Meadows *et al.* 1995; McGregor *et al.* 1995). The durations of the leaders are consistent with the elongations of the cometary comae over several tens of thousands of km observed prior to impact (Weaver *et al.* 1995). For the L event, a fainter feature was visible on the limb for at least 20 min prior to the impact, but it is not clear if this also represents 'leader' emission or

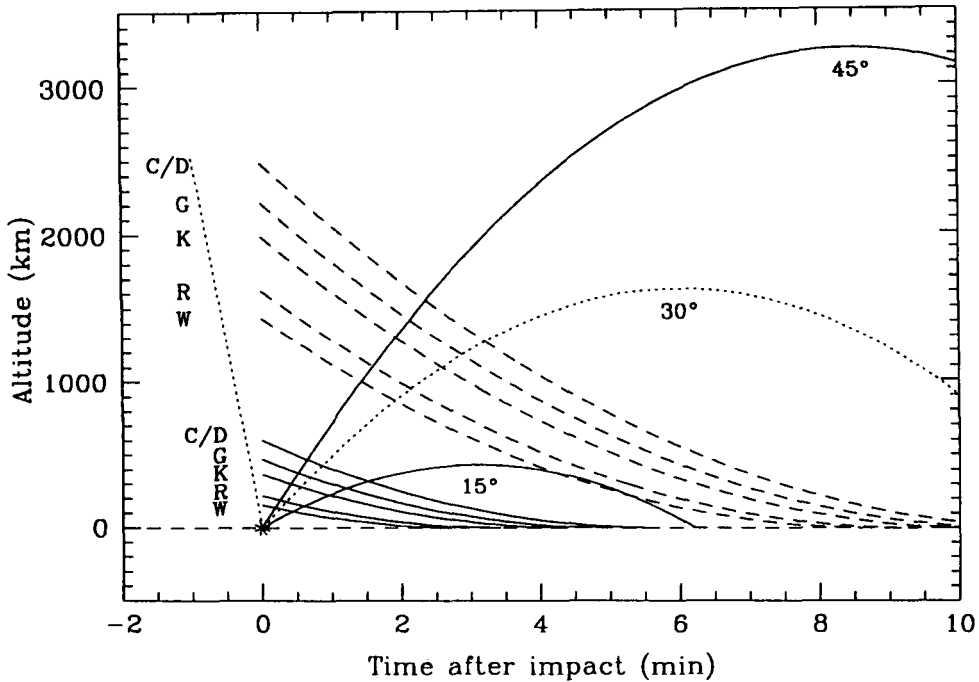


FIGURE 10. Plume altitude vs. time for an ejection velocity $v_e = 18 \text{ km s}^{-1}$ and ejection angles $\theta = 15^\circ, 30^\circ$ and 45° . Solid sloping lines indicate the altitude at which plume material becomes directly visible to an earth-based observer, for representative impacts, while the dashed lines indicate where the plume enters sunlight for the same impacts. The trajectory of the incoming fragments is shown by the dotted line at negative time. From McGregor *et al.* (1995).

the remnant of an earlier impact by an uncatalogued or lost (J?) fragment (Hamilton *et al.* 1995).

3.3. First precursor

First precursors have been identified convincingly only in the lightcurves for the G, H, K, L and R impacts, with the highest resolution data being available for the R, K and L events (Figs. 1, 8 & 9(a)). The first L precursor peaked sharply 7 sec prior to the initial Galileo PPR detection, declined to a plateau for about 8 sec, and then faded gradually over the next 40 sec (Hamilton *et al.* 1995). A similar pattern was observed for K, where the first precursor appeared abruptly and peaked 11 sec prior to the beginning of the flash observed by the Galileo SSI instrument (Watanabe *et al.* 1995), before decaying slowly over the next 60 sec. The first R precursor shows a similar development at $2.3 \mu\text{m}$, beginning abruptly ~ 24 sec prior to the Galileo NIMS flash, and then decaying slowly (Graham *et al.* 1995). The Siding Spring lightcurve for G shows but does not fully resolve the first precursor, which appears only as a 2-frame pause before it is overtaken by the second precursor (McGregor *et al.* 1995). In Calar Alto observations of the H impact, the first precursor appears in only four frames (Hamilton *et al.* 1995). For both G and H the initial abrupt flux increase occurs in the image obtained immediately prior to the onset of the corresponding Galileo flash, consistent with the higher-resolution K, L and R data.

The timing of the first precursor, as well as the steeply-brightening leader seen for L, strongly suggests that it was due to thermal emission from the main fragment as it entered Jupiter's upper atmosphere, 400–650 km above the effective impact level. Inspection of

Fig. 10 shows that the K and L meteors were indeed last directly visible above the limb at about this altitude. The ~ 10 sec gap between the first precursor peak and the onset of the Galileo flash represents the flight time of the bolide behind the jovian limb. The slow decay of the first precursor has been attributed to cooling of the heated trail left by the entering body (Hamilton *et al.* 1995; McGregor *et al.* 1995), while it has been suggested (Chapman 1995, private communication) that the plateau in the L data may be due to reflection of the initial fireball from infalling dust high in the atmosphere.

Finally, we note that a 30 sec exposure of the G impact taken by HST centered on the start time of the Galileo PPR/UVS flash (cf. Fig. 7 and Hammel *et al.* 1995) shows a point-like source of emission in the planet's shadow. Since the rising plume cannot have been visible at the Earth within 15 sec after the impact (see Fig. 10), this frame must also have captured the meteor during its passage through the upper atmosphere ~ 10 sec prior to impact.

3.4. *Second precursor*

Approximately 55–60 sec after the onset of the first precursor, a much brighter second precursor was seen for each of the larger impacts (cf. Figs. 1(b), 7, 8 & 9). In the case of the less energetic impacts such as A, C, D, Q2, Q1, S and W, only a single precursor was detected; we assume that this corresponds to the second precursor, although for the late W impact both precursors may have merged into a single event (McGregor *et al.* 1995). The rise time of the second precursor was 15–20 sec, and the duration (FWHM) was typically 30–60 sec. For the weaker impacts (*e.g.*, C, D, Q2, Q1 and W), the flux soon thereafter returned to the pre-impact level (cf. Fig. 3 and Herbst *et al.* 1995, Fig. 1).

For the bright G, H, K and L impacts, on the other hand, the flux level after the second precursor dipped only slightly and then remained relatively constant—or even increased slowly—for ~ 4 min until the main event began. The R impact presents a particularly interesting case, with the fluxes at 3.2 and 4.5 μm fading quite rapidly after the second precursor peaked, while the 2.3 μm flux declines only slowly (cf. Fig. 1(b)). A similar wavelength-dependence is shown by the H impact, where the flux was observed to drop more sharply after the second precursor at 3.1 μm than at 2.3 μm (Hamilton *et al.* 1995). Mid-IR observations of the H and L impacts show second precursors for these events at 10–12 μm , which also faded after 30–60 sec (Livengood *et al.* 1994; Lagage *et al.* 1995) in contrast to their persistence at 2.3 μm .

There is some indication that the time of peak flux for the second precursor is also wavelength-dependent, although results are inconsistent. Hamilton *et al.* (1995) found that the H precursor peaked 10–20 sec earlier at 3.1 μm than at 2.3 μm . Nicholson *et al.* (1995a) similarly noted that the R precursor began ~ 20 sec earlier at 4.5 μm than at 2.3 μm . However, Colas *et al.* (1995) find that the L precursor peaked ~ 15 sec later at 2.12 μm than at 1.25 or 1.65 μm . Drossart *et al.* (1995) and Lagage *et al.* (1995) note a 30 sec delay between the onset of the second L precursor at 2.3 μm and at 12 μm , although the second H precursor seems to have been seen essentially simultaneously at 2.3 μm and at 10 μm (Livengood *et al.* 1994). No obvious pattern emerges from these reports.

The second precursor has generally been interpreted as the first appearance of the fireball as seen from the Earth, rising above the jovian limb (*e.g.*, Graham *et al.* 1995). Comparison of the reported times for the second precursor with those of the initial Galileo flashes show that the 2.3 μm second precursors began 70 ± 18 sec (G), 48 ± 12 sec (H), 50 ± 7 sec (K), 39 ± 4 sec (L), 38 ± 11 sec (R) and 10 ± 16 sec (W) after the actual impact times (see chapter by Chodas & Yeomans). This pattern of decreasing intervals is consistent with the progressively shorter times taken by the rising fireball to reach an

altitude at which it is directly visible from earth, as illustrated in Fig. 10. The actual intervals between the impact flash and the arrival of the fireball at the limb also depend on jovian atmospheric extinction. Estimates of the pressure level at which the line-of-sight optical depth is of order unity range from ~ 15 mb at 2.3 or $3.5 \mu\text{m}$ (Meadows *et al.* 1995) to 100 mb at $10 \mu\text{m}$ (Livengood *et al.* 1995). These levels are, respectively, 90 km and 45 km above the 1 bar level, the approximate depth at which the explosion is believed to have been initiated (Boslough *et al.* 1995; Zahnle and MacLow 1995). Assuming a maximum vertical velocity of 12.5 km s^{-1} , and neglecting the initial acceleration phase of the explosion, we find that the G and H fireballs should have become visible at $2.3 \mu\text{m}$ no sooner than 40 sec after impact, while the R and W fireballs should have appeared after about 24 and 20 sec, respectively. These predictions are in reasonable agreement with the observed intervals quoted above.

This interpretation is strengthened by Galileo NIMS observations of the G impact, which clearly show a rising, cooling fireball at the same time as the second precursor was beginning (cf. Fig. 7). An HST image taken immediately after the Galileo flash had faded (at 7:35:16 UT) shows thermal emission in the planet's shadow from the rising plume. Near-IR spectra taken during the second precursor phase of the K impact show a blue continuum during the first minute of the second precursor, which then rapidly cooled over the succeeding few minutes (Meadows & Crisp 1995)—again consistent with a rising fireball.

The absence of any noticeable increase in brightness in the second precursors ~ 2 min after impact as the plumes crossed the terminator into sunlight (cf. Fig. 10) argues against any appreciable fraction of the near-IR flux at this time being due to reflected sunlight from condensates which may have formed in the plume.

In the context of a rising, cooling plume, the flat or slowly increasing flux level exhibited by the G, H, K and L precursors at $2.3 \mu\text{m}$ is puzzling. McGregor *et al.* (1995) have suggested that this may be due to the continued ejection of hot material from the entry site after the initial fireball for the most energetic (and deepest penetrating?) impacts. Some support for this explanation is provided by an HST image of the G plume taken at 7:38:16 UT, almost 5 min after the impact. This image appears to show the plume in sunlight, but with a faint 'tail' of thermal emission in the shadow region (Hammel *et al.* 1995). This tail could be interpreted in terms of continued ejection along the entry corridor. It is not clear, however, how the more rapid decay of the second precursors at $3.1 \mu\text{m}$ and longer wavelengths is to be interpreted in this context, as an increase in ejecta temperature over time seems rather unlikely. A similar problem arises in connection with the slow decay of the second R precursor at $2.3 \mu\text{m}$.

3.5. *Main event*

Approximately 6 min after each recorded impact, a steady and in some cases truly awesome brightening was observed at near-IR and mid-IR wavelengths. In the case of some of the smaller impacts, or when observing conditions were below par, this *main event* was the only feature observed. An initially rapid rise over 1 – 2 min was followed by a more gradual increase, the intensity reaching a peak 10 – 15 min after the moment of impact. The interval between impact and peak luminosity was correlated with the peak flux, the brighter events taking longer to reach maximum (Meadows *et al.* 1995); the average interval was 12 min. The initial decline in intensity following the peak had an e-folding time of ~ 3 min at $2.3 \mu\text{m}$, but was somewhat slower at 10 – $12 \mu\text{m}$ (cf. Figs. 3 and 4). In many cases the decay was interrupted by a plateau or *shoulder* at ~ 20 min after the impact.

At their peaks, the G and K fluxes at 2.3 μm probably both reached ~ 450 Jy, or 15 times the brightness of Io, although the G lightcurve is partly saturated. The peak brightness of the L impact seems to have been even greater, and this event strongly saturated the array detectors on larger telescopes. Observing at the 0.4 m telescope at Whately Observatory, Massachusetts, with an IR array and narrowband 2.30 μm filter, Skrutskie & Aas (1995) were able to follow the main L event through only modest saturation to a peak brightness of 35 times that of Io, or ~ 1000 Jy. Very similar main events were observed for impacts at 2.3, 3.1–3.2, 4.5, 10 and 12 μm , suggesting that the temperature of the emission remained relatively constant during the entire duration of this phase. At 12 μm the peak flux for the L impact reached 13,000 Jy, over 4 times the brightness of the H event and 8 times that of E and Q1 (cf. Fig. 4).

Although initial discussions of the main event for R (cf. Graham *et al.* 1995; Nicholson *et al.* 1995a) emphasized the rough coincidence between the time of peak flux and the time at which the impact site rotated onto the planet's limb, once a larger suite of observations became available it became apparent that this purely geometric interpretation of the lightcurves was not tenable. The extensive series of 2.3 μm lightcurves obtained at Siding Spring (McGregor *et al.* 1995; see Fig. 3), and the similar series of 12 μm lightcurves obtained at La Palma (Lagage *et al.* 1995; see Fig. 4), demonstrate conclusively that the main event began ~ 6 min after the impact time in *all* cases, irrespective of the distance of the impact point behind the limb. In fact, for the early C and D impacts, the main event was almost over by the time the impact site had rotated onto the limb (cf. dashed lines in Fig. 3). Moreover, the Galileo NIMS instrument recorded the beginning of the main events for G and R 370 sec after the initial flashes (Carlson *et al.* 1995a; 1995b), at almost exactly the same time as did earth-based observers at 2.3 μm (cf. Figs. 1 and 7). The average interval between the adopted impact time and the onset of the main event observed in 12 lightcurves (mostly at 2.3 μm) was 5.9 ± 0.3 min.

It is thus apparent that the origin of the main peak must be sought in the impact phenomenon itself, rather than in the observational geometry. The rapid adiabatic cooling of the rising plume makes it highly unlikely that the plume itself contributes significantly to thermal emission in the near-IR during the main event (Graham *et al.* 1995; Nicholson *et al.* 1995a), although this view has been disputed by Meadows *et al.* (1995) on the basis of spectroscopic evidence. Although several alternative suggestions have been made (*e.g.*, dust formation in the cooling plume—Hasegawa *et al.* 1995), the most likely explanation is that the tremendous burst of infrared flux is associated with the re-entry of the plume into the jovian atmosphere, where its kinetic energy is converted back to thermal energy via shock-heating (Zahnle & MacLow 1995; Boslough *et al.* 1995)—picturesquely described as the 'splashback' or 'hypervelocity splat'. Note that, because of the range of vertical ejection velocities represented in the plume, there is no contradiction in the lower velocity material beginning its re-entry at about the same time as the highest velocity material is nearing its peak altitude, as seen in the HST plume images (Boslough *et al.* 1995). Simple models for the infrared luminosity of the re-entering R impact plume have been generated by Zahnle and MacLow (1995), and are reviewed in the chapter by Zahnle in this volume. These models are quite successful in reproducing both the amplitude and the temporal evolution of the R main event at 2.3–4.5 μm , although it should be noted that the opacity source for the shock-heated debris is at present unknown and the model opacity was simply adjusted to fit the observations.

The common interval between impact and onset of the main event can be interpreted as requiring a minimum vertical re-entry velocity in order to generate significant shock-heating and/or thermal radiation. A 6 min flight time corresponds to a vertical velocity

component $v_z = gt/2 = 4.5 \text{ km s}^{-1}$. Zahnle (this volume) has in fact suggested that a minimum vertical re-entry velocity of $4\text{--}5 \text{ km s}^{-1}$ is needed to heat jovian air sufficiently for shock synthesis to produce abundant organic solids as opacity sources. At lower shock velocities, the heated gas remains transparent, and little IR radiation or organic aerosol production would be expected. As well as neatly explaining the 6 min delay of the main event, this hypothesis can also account for the hollow, crescent-shaped ejecta blankets observed by HST around the larger impact sites: material falling closer to the impact site does so at lower velocities, in general.

Given that the impacts occurred behind the planet's limb, and that the time for the impact site itself to rotate onto the limb ranged from 19 min for A to 9 min for W (see chapter by Chodas & Yeomans), it must be asked how the re-entering plume material could be seen by earth-based observers only 6 min after impact. The answer lies in the fact that most of the debris was apparently ejected not vertically upward, as in the simple 'toy plume' model of Zahnle & MacLow (1995), but in a south-easterly direction back along the inbound trajectory of the cometary fragments relative to the surface of Jupiter, and thus towards the limb. Although the simple ballistic model illustrated in Fig. 10 shows that material ejected at 45° elevation and our nominal ejection velocity of 18 km s^{-1} takes ~ 17 min to land, material ejected at lower velocities and on flatter trajectories lands sooner. Specifically, debris ejected at 18 km s^{-1} and $\theta = 15^\circ$ re-enters after only $2v_e \sin \theta/g = 6$ min, but remains in direct view of the Earth, *i.e.*, above the solid curves in Fig. 10. This is due in roughly equal parts to jovian rotation and downrange motion of the plume.

The overall duration of the typical main event of ~ 10 min fits well with the period during which plume material ejected at 18 km s^{-1} and elevations ranging from 15° to 45° would have landed. Some material may have been ejected at steeper elevations, but the maximum observed plume height of 3200 km (Hammel *et al.* 1995) sets an upper limit of $\sim 12.5 \text{ km s}^{-1}$ on the vertical velocity, and a corresponding upper limit of $2v_z/g = 17$ min on the ballistic flight time.

The relation between time-of-flight and longitudinal distance travelled by the plume material is shown more clearly in Fig. 11. For simplicity, the azimuth of ejection is assumed to be a constant 45° east of south, and the ejection velocity $v_e = 17.9 \text{ km s}^{-1}$. Points along the solid curve correspond to differing ejection angles θ , starting with $\theta = 0$ at the origin and increasing to $\theta = 45^\circ$ at the maximum range of 12,800 km (10.5° in longitude on Jupiter at latitude 44°S). (In reality, the full 3-dimensional plume involved a range of ejection velocities and azimuths as well, but these parameters are somewhat less important, within reasonable limits, in determining the maximum distance travelled downrange by the plume at any given time.) Horizontal dashed lines indicate significant events in the evolution of a typical impact plume: the start of the main event, the time at which the plume reaches maximum altitude, the time at which CO emission at $2.3 \mu\text{m}$ appears in the spectrum (Meadows & Crisp 1995), and the time of the shoulder in many lightcurves. Squares at $\theta = 15^\circ$ and $\theta = 30^\circ$ correspond approximately to the onset and peak of the main event, at which times the vertical velocity of the re-entering ejecta was 4.5 and 9 km s^{-1} , respectively.

Superimposed on the time-of-flight curve are a set of straight diagonal lines showing the distances of several representative impact sites behind the limb as functions of time from impact. At the intersection of the appropriate diagonal line with the time-of-flight curve, the expanding curtain of re-entering ejecta crosses the limb onto the visible face of Jupiter. Ejecta from the G impact, for example, began to land on the visible disk 6.3 min after impact, while that from the R impact crossed the limb within only 4.5 min.

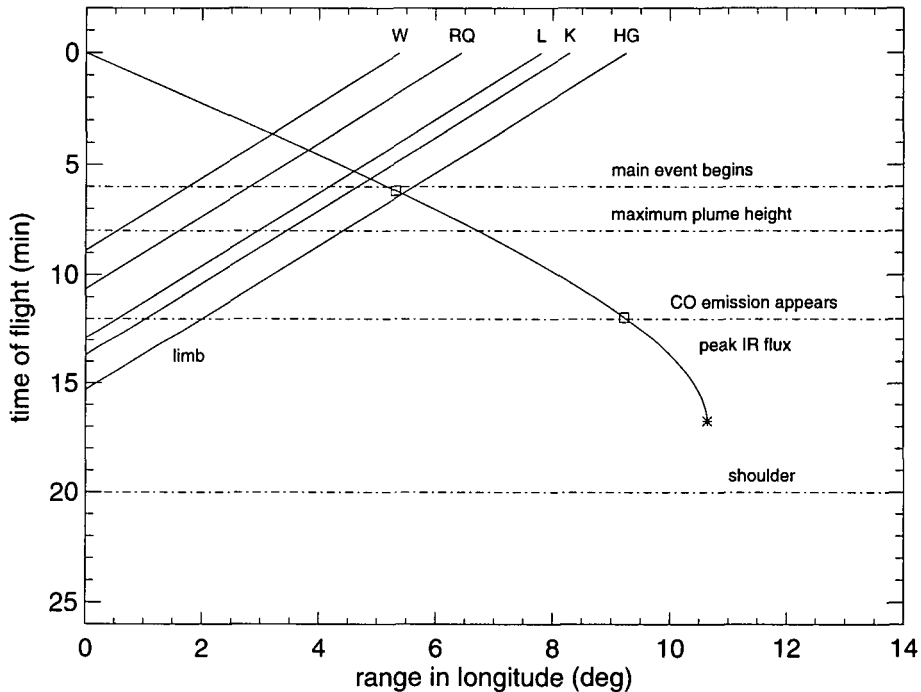


FIGURE 11. Time of flight vs. downrange distance (in longitude) for plume material ejected at $v_e = 17.9 \text{ km s}^{-1}$ and azimuth 45° east of south, for a range of elevation angles θ . An asterisk indicates the maximum range of 12,800 km (or 10.5° in longitude) reached by ejecta at $\theta = 45^\circ$, while the squares correspond to $\theta = 15^\circ$ and $\theta = 30^\circ$. Diagonal lines indicate where the falling ejecta crosses the limb onto the visible hemisphere of Jupiter.

The G and R impact sites themselves did not cross the limb until 15.5 min and 10.6 min, respectively, as indicated by the intercept of the diagonal lines on the vertical axis.

3.6. Shoulders

The declining phases of many of the SL9 lightcurves show shoulders, in the form of either changes in slope or even secondary maxima, 19–20 min after impact (see examples in Figs. 1, 3 and 4). These shoulders are seen both at $2.3 \mu\text{m}$ and at longer wavelengths. The R lightcurve also shows some evidence for subsequent, but more subdued shoulders at ~ 28 and 38 min after the impact; similar features are seen in the C and G lightcurves in Fig. 3.

The origin of these features is unclear. Suggestions that they are due to the impact ejecta crossing the terminator, and thus becoming visible in reflected light, run afoul of two facts: (i) the visibility of the shoulders at $12 \mu\text{m}$ as well as the near-IR, and (ii) the observation that they appear at a more-or-less fixed time interval after impact. Most other explanations involve a dynamical response of the atmosphere to the re-entering debris, either in the form of a vertically propagating sound wave reflected from the tropopause and/or the upper stratosphere (Livengood *et al.* 1995; Nicholson *et al.* 1995a), or an actual re-launching of some of the ejecta (MacLow 1994, private communication). A 1-dimensional ‘bounce’ model, powered by the adiabatic compression of the atmosphere under the weight of the collapsing plume, was explored numerically by Deming *et al.* (1995) who obtained an oscillation period of ~ 10 min, in good agreement with the observations. Their model, however, ignored radiative damping and may thus have overestimated the amplitude of the bounce. Two-dimensional hydrodynamical

models of the re-entering plume, including radiative losses, also show such a bounce (see chapter by MacLow in this volume).

4. Temperatures

Although a significant number of spectroscopic observations were made during several of the larger impacts, most of these data have yet to be published and few quantitative results are available at the time of writing. Compositional inferences from these measurements are reviewed in the chapter by Lellouch in this volume, while implications for the perturbed post-impact thermal structure of the jovian atmosphere are reviewed in the chapter by Conrath. We therefore restrict our discussion here to estimates of temperatures during the fireball and splashback phases, as these are of potential importance in constraining models of the impact process itself.

Temperature estimates may be divided into three categories, in order of decreasing probable reliability. First are physically-motivated spectroscopic estimates based, for example, on rotation-vibration line ratios. Even these estimates require a physical model for the emission region, and make assumptions of LTE, both of which may introduce significant errors (cf. discussion by Lellouch). Second are blackbody fits to regions of apparent continuum emission, perhaps representing the temperature of hot dust produced in the initial impact, or in the fallback shock. Figure 12 shows a series of medium-resolution grism spectra of the K impact obtained at the AAT which beautifully illustrate the evolution of the 2.0–2.4 μm spectrum during the fireball and splashback phases of this event (Meadows & Crisp 1995). Third are simple color temperatures derived from photometric flux ratios, which may suffer large systematic errors if the measured flux in one or more of the bands used is in fact dominated by line emission. We will group the available estimates by impact phase.

4.1. *First precursor (the bolide?)*

Very few multi-wavelength observations, and little spectroscopic data, have been reported for this short-lived phase in the lightcurves. Peak fluxes for the R impact first precursor at 2.3, 3.2 and 4.5 μm (cf. Fig. 1(b)) are consistent with a color temperature of 1000 ± 120 K (Nicholson *et al.* 1995b). A comparison of the flux measured by HST at 0.89 μm for what is interpreted as the meteor phase of the G impact (Hammel *et al.* 1995) with the simultaneously-measured first precursor brightness at 2.3 μm (cf. Fig. 7) yields a color temperature of 1800 K (McGregor *et al.* 1995). However, in both cases the measurements themselves were not made simultaneously, and it is likely that the fluxes changed appreciably during the integration times of 5–30 sec, casting considerable doubt on the reliability of the derived temperatures. The K impact spectrum at this time shows elevated emission longward of 2.05 μm , which matches a 6700 K blackbody (Fig. 12, panel 3).

4.2. *Second precursor (rising fireball)*

Thermal emission from the rising fireball was detectable for several minutes in the case of the larger impacts, permitting some spectroscopic observations. During most of the second precursor phase (Fig. 12, panels 4–6), the K impact spectra show primarily continuum emission with a blackbody temperature which declined from 720 K at $T_i + 3.5$ min to 420 K at $T_i + 6$ min. This presumably reflects the temperature of the plume after it had risen into view from the Earth; Galileo NIMS observations for the G and R impacts show considerably higher temperatures in the first 30 sec of the plume's development, when it was still hidden behind the limb (Carlson *et al.* 1995a).

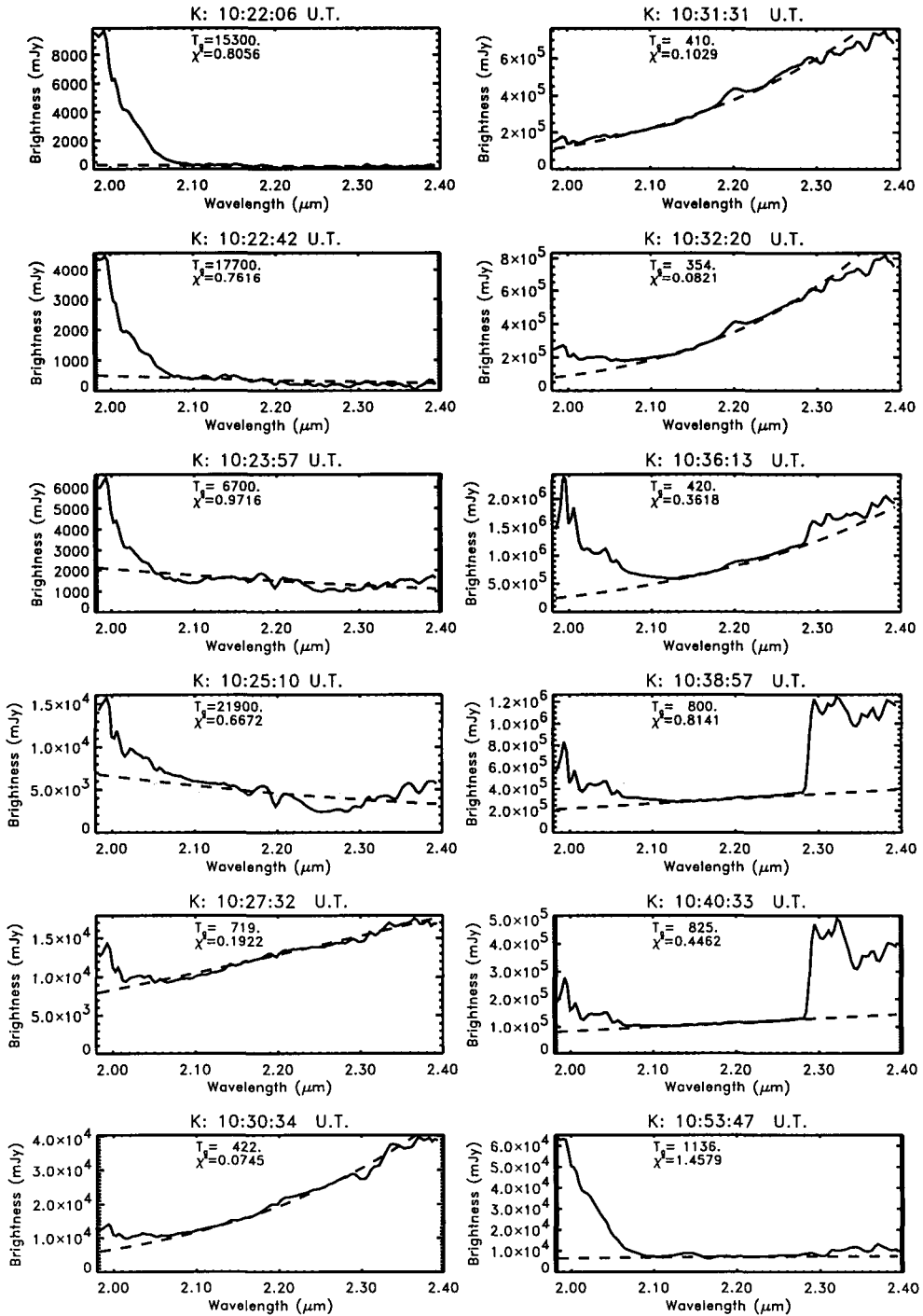


FIGURE 12. 2.0–2.4 μm spectra obtained at the Anglo-Australian Telescope during the K impact. Dashed curves indicate blackbody fits to the continuum regions of the spectra. The Galileo impact time was $T_i=10:24:13$ UT, while the main event began at $\sim 10:31$. Pre-impact leader emission is seen in panels 1 & 2, and the first precursor in panel 3. The second precursor begins in panel 4 and continues through panels 5 and 6. Panels 7–11 cover the main event, with panel 9 at $T_i + 12$ min falling near the peak of the 2.3 μm lightcurve. Absolute calibration is provisional. Adapted from Meadows & Crisp (1995).

Color temperatures derived from 2.3/3.1 μm flux ratios during the latter part of the H second precursor are 900–1300 K (Hamilton *et al.* 1995), while during the equivalent phase of the R impact the 2.3/4.5 μm color temperature slowly increased from 650 K at $T_i + 1$ min to 850 K at $T_i + 3.5$ min. Spanning a wider wavelength range, measurements of the H and L precursor peaks at 10 and 12 μm (Livengood *et al.* 1995; Lagage *et al.* 1995) combined with data at 2.3 μm imply similar color temperatures of 600–625 K.

4.3. *Main event (collapsing plume)*

In the early stages of the main event, the 2.0–2.4 μm spectrum of the K impact continued to be dominated by continuum emission, with temperatures of ~ 400 K. Beginning near the time of peak flux, and for ~ 10 min thereafter, prominent CO emission was observed longward of 2.30 μm , with NH_3 and possible H_2O emission below 2.1 μm (Meadows & Crisp 1995). Similar CO emission was observed in near-IR spectra of the C, D, G, H, R and W impacts (Meadows & Crisp 1995; Herbst *et al.* 1995). Excitation of these $\Delta\nu = 2$ vibrational bands usually implies a temperature of 2000 K or higher. The NH_3 emission implies a similarly high temperature, although Lellouch cautions against such a simple LTE-based interpretation. In contrast, fits to the emission by H_2O at 2.04 μm in the spectra at the K peak suggest a temperature of 600–700 K (Meadows & Crisp 1995), while Encrenaz *et al.* (1995) estimate a temperature of 750 K at the peak of the H lightcurve, based on CH_4 spectra at 3.5 μm and an assumed effective pressure level for the radiating region of 1 mb. Maillard *et al.* (1995) derived a temperature of 750–1500 K at the peak of the C lightcurve from CH_4 emission lines at 3.3 μm . The onset of CO emission may signal the increasing vertical re-entry velocity of the plume, $v_z = gt/2$: by $T_i + 12$ min this had reached 9 km s^{-1} .

Bjoraker *et al.* (1995), using the Kuiper Airborne Observatory with an echelle grating spectrometer at 7.7 μm , observed the main events for the G and K impacts. Emission due to hot methane, water and dust was observed to commence ~ 7 min after the K impact, peak at 13–14 min post-impact, and then decay by ~ 25 min. A temperature of ~ 1000 K and a base pressure of 3 μb at the K peak was derived from the relative strengths of hot H_2O and CH_4 lines. Lower-resolution 5–10 μm spectroscopic observations were also made with the KAO for the R and W impacts by Sprague *et al.* (1995), revealing strong emission by CH_4 and H_2O at a temperature of ~ 500 K.

Simultaneous monitoring of the R lightcurve at 3.2 and 4.5 μm showed a surprisingly constant color temperature of ~ 1000 K during the fallback phase, although this may be strongly affected by CH_4 line emission at 3.2 μm . In fact, the best overall fit to the R impact spectrum from 2.3 to 13 μm at the time of peak flux implies either a blackbody at 700 K, or an opacity which scales as λ^{-1} , as expected for emission by sub-micron dust particles, and $T \sim 600$ K (Nicholson *et al.* 1995b). Simultaneous narrowband measurements at 7.85, 10.3 and 12.2 μm by Friedson *et al.* (1995) are also consistent with this fit (cf. Fig. 13).

Color temperatures derived from published lightcurves at 2.3 and 10–12 μm for the E, H, L and R impacts, evaluated at the time of peak flux, also fall in the range 550–700 K. Of course, these estimates may be systematically skewed by CO emission at 2.3 μm and/or silicate emission at 10 μm (Nicholson *et al.* 1995b). Perhaps none of the above blackbody temperature estimates should be taken too seriously until a physical model of the emission from the shocked mixture of cometary debris and jovian atmosphere is developed which takes into account both molecular and dust emission, as well as the near-limb viewing geometry.

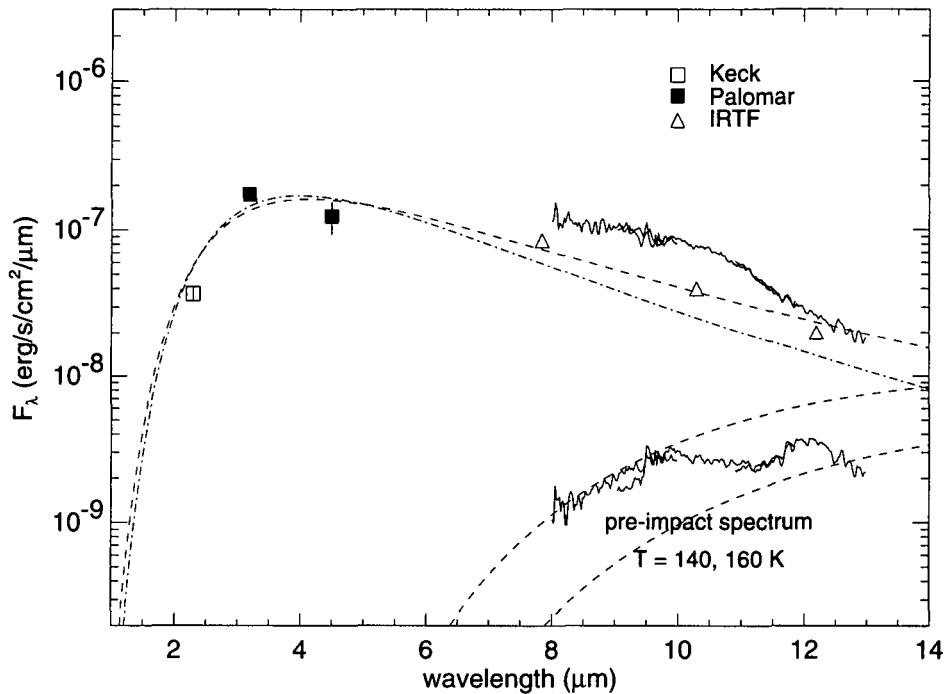


FIGURE 13. Composite spectrum for the R impact, at the peak of the main event, based on narrowband imaging at 2.3, 3.2, 7.85, 10.3 and 12.2 μm , broadband imaging at 4.5 μm , and low-resolution spectroscopy at 8–13 μm . Data from Nicholson *et al.* (1995a), Graham *et al.* (1995) and Friedson *et al.* (1995). The dashed curve shows the best-fitting blackbody spectrum (700 K, with an optical depth-solid angle product $\Omega\tau = 0.01$ sq arcsec), while the dot-dashed curve is the best-fitting dust-opacity ($\tau \sim \lambda^{-1}$) model, with $T = 600$ K and $\Omega\tau = 0.01$ sq arcsec at 10 μm . The spectrum at lower right was obtained immediately prior to the impact, and reflects normal jovian tropospheric and lower stratospheric temperatures of 140–160 K. Adapted from Nicholson *et al.* (1995b).

5. Anomalous lightcurves

A few apparently aberrant lightcurves do not appear to fit comfortably into the scenario described in §3. The strong Q1 precursor, similar in shape to the second L precursor, is reported to have started 37 sec *before* the initial Galileo PPR detection (Herbst *et al.* 1995), an anomaly with no obvious explanation.

The Q2 impact, which occurred 29 min before Q1, showed a single precursor followed about 8 min later by a very subdued ‘main event’, which was fainter than the precursor (Herbst *et al.* 1995).

The V impact was observed only as a brief flash, ~ 30 sec in duration, with no subsequent main event at all (Weinberger 1994; Meadows 1994, private communications). Based on its duration and its similarity to the first R precursor at 2.3 μm (Fig. 14), we tentatively identify this as a ‘first precursor’, perhaps due to the entry flash of a particularly small and/or weak fragment of SL9.

For each of the B, M and N impacts, there is a single report of a brief (1–2 min in duration) period of weak 2.3 μm emission (de Pater 1994, private communication; McGregor *et al.* 1995), which most likely reflects a very faint main event with no discernable precursor. The N event was first seen at 10:36:30 UT, 7 min after the impact flash was detected by the Galileo SSI instrument, consistent with a barely-detectable main event.

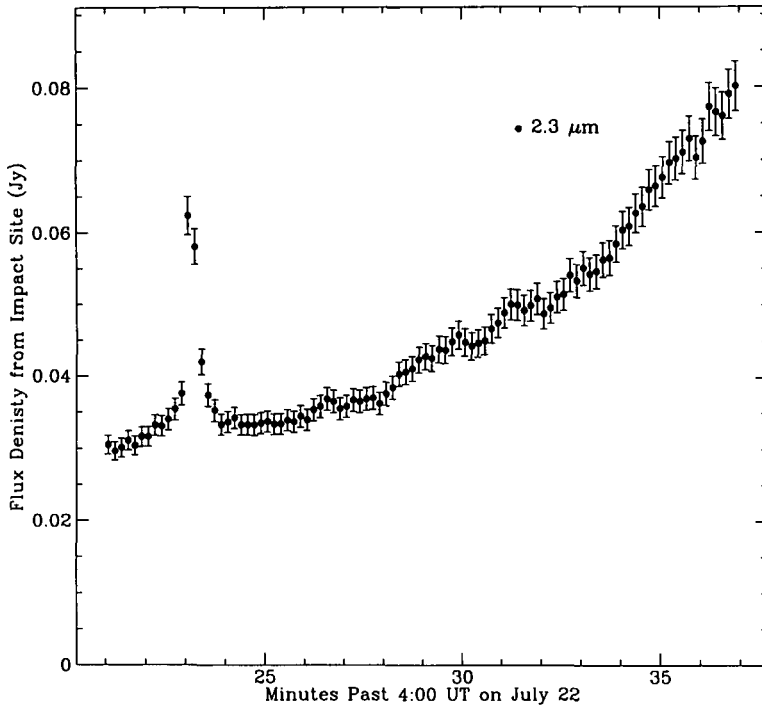


FIGURE 14. Palomar lightcurve showing the very brief V impact flash at $2.3 \mu\text{m}$, at 10 sec resolution. The increasing background signal is due to the old E impact site rotating across the terminator. A simultaneous flash was recorded at the AAT. Possible faint leader emission is seen before the main flash, but there appears to have been no detectable 'main event'. Unpublished data from A. Weinberger.

A similar report of a faint U event was made by Cochran *et al.* (1995), but simultaneous observations with larger telescopes under clear skies failed to detect any signature of this impact (Hamilton *et al.* 1995). Likewise, early reports of an F impact have not been confirmed by other observers, and were likely due to confusion with the re-appearance of the old E impact site on the limb.

6. Other phenomena

6.1. Satellite flashes

Considerable attention before and during the SL9 impacts was devoted to predicting and searching for impact flashes reflected from the Galilean satellites. Despite several efforts to record a reflected flash with photometers and CCD cameras, no unambiguous reflected signals were detected. Consolmagno & Menard (1995) monitored Europa during the A impact and Europa during the H, Q1 and Q2 impacts. Possible $2\text{-}\sigma$ detections of flashes from A, Q2 and Q1 were reported, but none was considered to be convincing. A'Hearn *et al.* (1995) and Woodney *et al.* (1995) report observations of Io and Europa during the D, E and K impacts, and derive upper limits on the peak flash luminosity at 0.42 and $0.62 \mu\text{m}$. However, the D and E limits far exceed the peak luminosities measured by the Galileo PPR and SSI instruments for several brighter impacts. It is apparent from these results that the flashes—particularly when reflected from sunlit satellites—were far too faint for detection at visual wavelengths.

A more favourable opportunity was provided by the K impact, which occurred while Europa was in eclipse but visible to earth-based observers if illuminated by the flash.

However, no detectable visual signal was observed, and the flux at $2.34 \mu\text{m}$ did not exceed 6 mJy (McGregor *et al.* 1995). Both visible and near-IR upper limits on the K flash exceed by a factor of ~ 10 those expected based on the peak luminosity measured by the Galileo SSI experiment, assuming isotropic emission and temperatures of several thousand K.

6.2. *Post-impact features on Jupiter*

Due to the strong methane absorption in the underlying atmosphere, the ejecta blankets deposited by the larger impacts were readily visible in reflected sunlight as bright features in images taken at wavelengths of 2.3 or $3.5 \mu\text{m}$. The structure of the ejecta blankets is best seen in the HST images (cf. chapter by Hammel in this volume), but some information concerning the impact process itself may be gleaned from the near-IR images. Although the impact site was generally unresolved in images taken near the peak of the main event, implying a source size of order 4000 km or less, later images frequently showed an extended region of emission, elongated along the planet's limb (Graham *et al.* 1995; Nicholson *et al.* 1995a; Lagage *et al.* 1995). Dimensions ranged from ~ 8000 km for the R impact at 2.3 and $4.5 \mu\text{m}$ to $30,000$ km for L at $12 \mu\text{m}$. The smaller measurement is compatible with the size of the ejecta blankets imaged in the visible by HST (Hammel *et al.* 1995).

Near-IR images of several sites taken during the impact week show a distinct central spot and a crescent-shaped feature to the south-east, reminiscent of the celebrated HST image of the G site (West *et al.* 1995). Although only a few quantitative analyses have yet been performed using these data (Banfield *et al.* 1995; Chanover *et al.* 1995; Ortiz *et al.* 1995; Moreno *et al.* 1995), it is clear that the ejecta was deposited fairly high in the stratosphere, at pressure levels of 10 mb or less. For more details, see the chapter by West in this volume.

6.3. *Three-micron rings*

More unexpected was the discovery of very large circular rings surrounding the C, G and K impact sites and visible only between 3.1 and $4.0 \mu\text{m}$ (McGregor *et al.* 1995). Over this range, their spectra are extremely blue. Measurements of re-projected images show that the G and K rings expanded at a rate of $\sim 1400 \text{ m s}^{-1}$ to radii of $\sim 18,500$ km 2 hr after the impacts, before slowly fading from view 1.5 hrs later. No sign of these features is seen in many images taken at shorter wavelengths. The rings are centered ~ 3500 km to the south-east of the impact sites, in the same direction as the displacement of the HST ejecta patterns, and appear to have expanded from an initial radius of ~ 8000 km, within the optical crescent. It is not clear if the rings are seen in emission or reflected sunlight, although the former seems more consistent with the rapid fading. Their spectral signature is consistent with emission by poly-HCN (P. Wilson 1995, private communication). These rings are quite distinct from the expanding waves seen in the HST images of several sites; the latter are restricted to radii of 5000 km or less and expanded at a much slower rate of 450 m s^{-1} (Hammel *et al.* 1995).

Although no good model exists for these features, it has been suggested (Zahnle 1995, private communication) that they could be due to impact debris 'sliding' horizontally across the top of the atmosphere, from an initial location in the crescent. Alternative explanations include mildly supersonic shock waves propagating in the stratosphere, where the sound speed is $\sim 980 \text{ m s}^{-1}$.

7. Summary

Despite some predictions to the contrary, almost all phases of the impact process—with the exception of the terminal phase of the bolide and the initial seconds of the fireball—were apparently recorded by ground-based instruments. Although we are still far from having quantitative models which successfully account for all the features observed in the SL9 impact lightcurves, a viable qualitative picture of the various impact phenomena does seem to have emerged, capable of explaining the principal observations. A remarkably consistent set of characteristics emerges for the best-observed events, beginning with the first and second precursor flashes as the bolide entered the jovian atmosphere and the hot fireball emerged from behind the limb, and culminating in the infrared main event as the ejecta plume re-entered the jovian atmosphere. Only a handful of weaker events failed to follow this pattern. A simple ballistic plume model is successful in accounting for the timing of the major features in the lightcurves; in the future more realistic 3-D hydrodynamic simulations will be required to model quantitatively the observed fluxes and extract fragment energies, penetration depths, re-entry altitudes, etc. Particular problems include the persistence of the second precursor for the larger impacts, and the multiple shoulders exhibited by several lightcurves.

A general correlation is observed between the peak brightness of the infrared signal and the estimated sizes of the pre-impact fragments, and with the morphology of the post-impact sites as seen in the HST images. The faintest (or undetected) impact signatures were associated with fragments displaced from the main SL9 train, strongly suggesting that some 'fragments' were little more than fluffy aggregates, or perhaps simply agglomerations of dust.

Temperature estimates derived from near-IR and mid-IR photometry and spectroscopy range from 1000 K or higher for the entry trail of the bolide, through ~ 750 K for the fireball after it had cleared the limb. Temperatures derived during the splashback phase are less concordant, varying from 500 K to 2000 K. This dispersion may reflect a combination of non-LTE effects, non-blackbody emission, and real temperature variations, both spatial and temporal. Development of more realistic radiative models for the re-entering plume is clearly a high priority if the wealth of available spectroscopic and color data is to be fully interpreted.

Over the year since the events of July 1994 the author has greatly benefitted from discussions with many individuals, and it is impossible at this date to attribute correctly all original ideas. Much of the impact scenario presented here was developed in discussions at the AAS Division for Planetary Sciences conference in October 1994 and the European SL9 meeting in February 1995, and refined during IAU Colloquium 156 in May 1995. Particular thanks go to Don Banfield, Clark Chapman, Paul Chodas, Imke de Pater, Doug Hamilton, Tom Hayward, Peter McGregor, Keith Matthews, Vikki Meadows, Gerry Neugebauer, Glenn Orton, Alycia Weinberger, Kevin Zahnle and, last but not least, Audrey and Alicia. Preparation of this article was supported by the NSF and the NASA Planetary Astronomy program.

REFERENCES

- A'HEARN, M. F., MEIER, R., WELNITZ, D., AND WOODNEY, L. 1995 Were Any Impact Flashes Seen in Reflection from the Satellites? In *Proceedings of the European SL-9/Jupiter Workshop* (eds. R. West and H. Bohnhardt) pp. 113–118. ESO.

- BANFIELD, D., GIERASCH, P., SQUYRES, S. W., NICHOLSON, P. D., CONRATH, B. AND MATTHEWS, K. 1995 2 μm Spectrophotometry of Jovian Stratospheric Aerosols—Scattering Opacities, Vertical Distributions and Wind Speeds. *Icarus*, (submitted).
- BJORAKER, G. L., STOLOVY, S. R., HERTER, T. L., GULL, G. E. AND PIRGER, B. E. 1995 Detection of Water After the Collision of Fragments G and K of Comet Shoemaker-Levy 9 with Jupiter. *Science* (submitted).
- BOSLOUGH, M., CRAWFORD, D., ROBINSON, A., AND TRUCANO, T. 1994 Mass and penetration depth of Shoemaker-Levy 9 fragments from time-resolved photometry. *Geophys. Res. Lett.* **21**, 1555.
- BOSLOUGH, M., CRAWFORD, D., TRUCANO, T., AND ROBINSON, A. 1995 Numerical modeling of Shoemaker-Levy 9 impacts as a framework for interpreting observations. *Geophys. Res. Lett.* **22**, 1821.
- CARLSON, R. W., WEISSMAN, P. R., SEGURA, M., HUI, J., SMYTHE, W. D., JOHNSON, T., BAINES, K. H., DROSSART, P., ENCRENAZ, TH., AND LEADER, F. E. 1995a Galileo infrared observations of the Shoemaker-Levy 9 G impact fireball: A preliminary report. *Geophys. Res. Lett.* **22**, 1557.
- CARLSON, R. W., WEISSMAN, P. R., HUI, J., SMYTHE, W. D., BAINES, K. H., JOHNSON, T. V., DROSSART, P., ENCRENAZ, T., LEADER, F. E. AND MEHLMAN, R. 1995b Some timing and spectral aspects of the G and R collision events as observed by the Galileo near-infrared mapping spectrometer. In *Proceedings of the European SL-9/Jupiter Workshop* (eds. R. West and H. Bohnhardt) pp. 69–73. ESO.
- CHANOVER, N. J., BEEBE, R. F., MURRELL, A. S., AND SIMON, A. A. 1995 Absolute Reflectivity Spectra of Jupiter: 0.25–3.5 Microns. *Icarus*, (submitted).
- CHAPMAN, C. R., MERLINE, W. J., KLAASEN, K., JOHNSON, T. V., HEFFERNAN, C., BELTON, M. J. S., INGERSOLL, A. P., AND THE GALILEO IMAGING TEAM 1995 Preliminary results of Galileo direct imaging of S-L 9 Impacts. *Geophys. Res. Lett.* **22**, 1561.
- COCHRAN, A. L., ARMOSEY, B. J., PULLIAM, C. E., CLARK, B. E., COCHRAN, W. E., FRUEH, M., LESTER, D. F., TRAFTON, L., KIM, Y., NA, C., AND PRYOR, W. 1995 An Update on Imaging Observations from McDonald Observatory. In *IAU Colloquium 156: The Collision of Comet P/Shoemaker-Levy 9 and Jupiter*, p. 21.
- COLAS, F., TIPHENE, D., LECACHEUX, J., DROSSART, P., DEBATZ, D., PAU, S., ROUAN, D., AND SEVRE, F. 1995 Near-infrared imaging of SL9 impacts on Jupiter from Pic-du-Midi Observatory. *Geophys. Res. Lett.* **22**, 1765.
- CONSOLMAGNO, G. J. AND MENARD, G. 1995 A search for variations in the light curves of Io and Europa during the impact of Comet SL9: A, H, and Q events. *Geophys. Res. Lett.* **22**, 1633.
- CRAWFORD, D., BOSLOUGH, M., TRUCANO, T., AND ROBINSON, A. 1994. The impact of comet Shoemaker-Levy 9 on Jupiter. *Shock Waves*, **4**, 47.
- DEMING, D AND HARRINGTON, J. 1995. no title; poster paper at IAU Colloquium 156, Baltimore MD.
- DROSSART, P., ENCRENAZ, T., LECACHEUX, J., COLAS, F., AND LAGAGE, P.O. 1995 The time sequence of SL9/impacts H and L from infrared observations. *Geophys. Res. Lett.* **22**, 1769.
- ENCRENAZ, T., SCHULZ, R., STÜWE, J. A., WIEDEMANN, G., DROSSART, P., AND CROVISIER, J. 1995 Near-IR spectroscopy of Jupiter at the time of SL9 impact: Emissions of CH₄, H₃⁺, and H₂. *Geophys. Res. Lett.* **22**, 1577.
- FRIEDSON, A. J., HOFFMANN, W. F., GOGUEN, J. D., DEUTSCH, L. K., ORTON, G. S., HORA, J. L., DAYAL, A., SPITALE, J. N., WELLS, W. K., AND FAZIO, G. G. 1995 Thermal infrared lightcurves of the impact of comet Shoemaker-Levy 9 Fragment R. *Geophys. Res. Lett.* **22**, 1569.
- GRAHAM, J., DE PATER, I., JERNIGAN, J., LIU, M., AND BROWN, M. 1995. W. M. Keck telescope observations of the comet P/Shoemaker-Levy 9 fragment R Jupiter collision. *Science* **267**, 1320.

- HAMILTON, D. P., HERBST, T. M., RICHICHI, A., BÖHNHARDT, H., ORTIZ, J. L. 1995 Calar Alto Observations of Shoemaker-Levy 9: Characteristics of the H and L Impacts. *Geophys. Res. Lett.* **22**, 2417.
- HAMMEL, H. B., BEEBE, R. F., INGERSOLL, A. P., ORTON, G. S., MILLS, J. R., SIMON, A. A., CHODAS, P., CLARKE, J. T., DE JONG, E., DOWLING, T. E., *et al.* 1995 HST Imaging of Atmospheric Phenomena Created by the Impact of Comet Shoemaker-Levy 9. *Science* **267**, 1288.
- HASEGAWA, H., TAKEUCHI, S., WATANABE, J. 1995 Grain Formation in Cometary Impact Plume. In *Proceedings of the European SL-9/Jupiter Workshop* (eds. R. West and H. Bohnhardt) pp. 279–286. ESO.
- HERBST, T. M., HAMILTON, D. P., BÖHNHARDT, H., AND ORTIZ-MORENO, J. L. 1995 Near Infrared Imaging and Spectroscopy of the SL-9 Impacts from Calar Alto. *Geophys. Res. Lett.* **22**, 2413.
- HORD, C. W., PRYOR, W. R., STEWERT, A. I. F., SIMMONS, K. E., GEBBEN, J. J., BARTH, C. A., MCCLINTOCK, W. E., ESPOSITO, L. W., TOBISKA, W. K., WEST, R. A., ED-
BERG, S. J., AJELLO, J. M. AND NAVIAUX, K. L. 1995 Direct observations of the comet Shoemaker-Levy 9 fragment G impact by Galileo UVS. *Geophys. Res. Lett.* **22**, 1565.
- LAGAGE, P. O., GALDEMARD, PH., PANTIN, E., JOUAN, R., MASSE, P., SAUVAGE, M., OLOF-
SSON, G., HULDTGREN, M., NORDH, L., BELMONTE, J. A., REGULO, C., RODRIGUEZ
ESPINOSA, J. M., VIDAL, L., MOSSER, B., ULLA, A., AND GAUTIER, D. 1995 SL-9 frag-
ments A, E, H, L, Q1 collision on to Jupiter: Mid-infrared light curves. *Geophys. Res. Lett.* **22**, 1773.
- LIVENGOOD, T. A., KÄUFL, H. U., KOSTIUK, T., BJORAKER, G. L., ROMANI, P. N., WIEDE-
MANN, G., MOSSER, B., AND SAUVAGE, M. 1995 Multi-Wavelength Thermal-Infrared
Imaging of SL9 Impact Phenomena. In *Proceedings of the European SL-9/Jupiter Workshop*
(eds. R. West and H. Bohnhardt) pp. 1437–146. ESO.
- MAILLARD, J. P., DROSSART, P., BÉZARD, B., DE BERGH, C., LELLOUCH, E., MARTEN,
A., CALDWELL, J., HILICO, J. C. 1995 Methane and carbon monoxide infrared emissions
observed at the CFH telescope during the collision of comet SL-9 on Jupiter. *Geophys. Res.
Lett* **22**, 1573.
- MARTIN, T. Z., ORTON, G. S., TRAVIS, L. D., TAMPPARI, L. K., AND CLAYPOOL, I. 1995 Ob-
servation of Shoemaker-Levy Impacts by the Galileo Photopolarimeter radiometer. *Science*
268, 1875.
- MCGREGOR, P., NICHOLSON, P. D., AND ALLEN, M. 1995. CASPIR observations of the collision
of Comet Shoemaker-Levy 9 with Jupiter. *Icarus*, (submitted).
- MEADOWS, V. AND CRISP, D. 1995 Impact Plume Composition from Near-Infrared Spec-
troscopy. In *Proceedings of the European SL-9/Jupiter Workshop* (eds. R. West and
H. Bohnhardt) p. 239. ESO.
- MEADOWS, V., CRISP, D., ORTON, G., BROOKE, T., AND SPENCER, J. 1995 AAT IRIS Obser-
vations of the SL-9 Impacts and Initial Fireball Evolution. In *Proceedings of the European
SL-9/Jupiter Workshop* (eds. R. West and H. Bohnhardt) p. 233. ESO.
- MORENO, F., MUNOZ, O., MOLINA, A., LOPEZ-MORENO, J. J., ORTIZ, J. L., RODRIGUEZ, J.,
LOPEZ-JIMINEZ, A., GIRELA, F., LARSON, S. M. AND CAMPINS, H. 1995 Physical prop-
erties of the aerosol debris generated by the impact of fragment H of comet P/Shoemaker-
Levy 9 on Jupiter. *Geophys. Res. Lett.* **22**, 1609.
- NICHOLSON, P. D., GIERASCH, P. J., HAYWARD, T. L., MCGHEE, C. A., MOERSCH, J. E.,
SQUYRES, S. W., VAN CLEVE, J., MATTHEWS, K., NEUGEBAUER, G., SHUPE, D., WEIN-
BERGER, A., MILES, J. W., AND CONRATH, B. J. 1995a Palomar observations of the
impact of fragment R of comet P/Shoemaker-Levy 9: I. Light curves. *Geophys. Res. Lett.*
22, 1613.
- NICHOLSON, P. D., GIERASCH, P. J., HAYWARD, T. L., MCGHEE, C. A., MOERSCH, J. E.,
SQUYRES, S. W., VAN CLEVE, J., MATTHEWS, K., NEUGEBAUER, G., SHUPE, D., WEIN-
BERGER, A., MILES, J. W. AND CONRATH, B. J. 1995b Palomar observations of the impact
of fragment R of comet P/Shoemaker-Levy 9: II. Spectra. *Geophys. Res. Lett.* **22**, 1617.

- ORTIZ, J. L., MUNOZ, O., MORENO, F., MOLINA, A., HERBST, T. M., BIRKLE, K., BÖHNHARDT, H., AND HAMILTON, D. P. 1995 Models of the Shoemaker-Levy 9 Collision Generated Hazes. *Geophys. Res. Lett.* **22**, 1605.
- ORTON, G., A'HEARN, M., BAINES, K., DEMING, D., DOWLING, T., GOGUEN, J., GRIFFITH, C., HAMMEL, H., HOFFMANN, W., HUNTEN, D., JEWITT, D., KOSTIUK, T., *et al.* 1995 Collision of Comet Shoemaker-Levy 9 with Jupiter Observed by the NASA Infrared Telescope Facility. *Science* **267**, 1277.
- SEKANINA, Z., CHODAS, P. W., AND YEOMANS, D. K. 1994 Tidal Disruption and the Appearance of Periodic Comet Shoemaker-Levy 9. *Astron. & Astrophysics* **289**, 607.
- SKRUTSKIE, M. F., AND AAS, S. 1995 A 2.3 μm Light Curve of the "L" impact. *Icarus* (submitted).
- SPRAGUE, A., BJORAKER, G., HUNTEN, D., WITTEBORN, F., KOZLOWSKI, R., AND WOODEN, D. 1995. Observations of H₂O following the R and W impacts of comet Shoemaker-Levy 9 into Jupiter's atmosphere. *Icarus* (in press).
- TAKATA, T., O'KEEFE, J. D., AHRENS, T. J., AND ORTON, G. 1994 Comet Shoemaker-Levy 9: Impact on Jupiter and plume evolution. *Icarus* **109**, 3.
- TAKEUCHI, S., HASEGAWA, H., WATANABE, J., YAMASHITA, T., ABE, M., HIROTA, Y., NISHIHARA, E., OKUMURA, S., AND MORI, A. 1995 Near-IR imaging observations of the cometary impact into Jupiter: Time variation of radiation from impacts of fragments C, D, and K. *Geophys. Res. Lett.* **22**, 1581.
- WATANABE, J., YAMASHITA, T., HASEGAWA, H., TAKEUCHI, S., ABE, M., HIROTA, Y., NISHIHARA, E., OKUMURA, S., AND MORI, A. 1995 Near-IR Observation of Cometary Impacts to Jupiter: Brightness Variation of the Impact Plume of Fragment K. *Publ. Astron. Soc. Japan* **47**, L21.
- WEAVER, H. A., A'HEARN, M. F., ARPIGNY, C., BOICE, D. C., FELDMAN, P. D., LARSON, S. M., LAMY, P., LEVY, D. H., MARSDEN, B. G., MEECH, K. J., NOLL, K. S., *et al.* 1995 The Hubble Space Telescope (HST) Observing Campaign on Comet Shoemaker-Levy 9. *Science* **267**, 1282.
- WEST, R. A., KARKOSCHKA, E., FRIEDSON, A. J., SEYMOUR, M., BAINES, K. H., AND HAMMEL, H. B. 1995 Impact Debris Particles in Jupiter's Stratosphere. *Science* **267**, 1296.
- WOODNEY, L. M., MEIER, R., A'HEARN, M. F., WELLNITZ, D., SMITH, T., VERVEER, A., AND MARTIN, R. 1995 Photometry of the Jovian Satellites During Comet D/Shoemaker-Levy 9's Impact with Jupiter. *DPS meeting abstract*.
- ZAHNLE, K., AND MACLOW, M. M. 1994 The collision of Jupiter and Comet Shoemaker-Levy 9. *Icarus* **108**, 1.
- ZAHNLE, K., AND MACLOW, M. M. 1995. A simple model for the light curve generated by a Shoemaker-Levy 9 impact. *J. Geophys. Res.* **100**, 16885.